Ore Geology Reviews 139 (2021) 104535

Contents lists available at ScienceDirect

Ore Geology Reviews

journal homepage: www.elsevier.com/locate/oregeorev

Timing and genesis of the Tudiling trachyte Nb-Ta-Zr-REE deposit in the South Qinling (Central China): Implications for rare metal enrichment in extrusive peralkaline magmatic systems

Shuang Yan [a,b], Qiang Shan [a,b,*], He-Cai Niu [a,b], Xueyuan Yu [a,b], Xu Zhao [a,b], Xiao-Chen Zhao [a,b], Hai-Jun Zhang [c], Yilin Xiong [d]

[a] CAS Key Laboratory of Mineralogy and Metallogeny/Guangdong Provincial Key Laboratory of Mineral Physics and Materials, Guangzhou Institute of Geochemistry, Chinese Academy of Sciences, Guangzhou 510640, China
[b] CAS Center for Excellence in Deep Earth Science, Guangzhou, 510640, China
[c] Wuhan Center, China Geological Survey, Wuhan 430205, China
[d] Hubei Geological Survey, Wuhan 430034, China

ARTICLE INFO

Keywords:
Peralkaline trachyte
Emplacement timing
Genesis
Rare metal mineralization
South Qinling

ABSTRACT

Relative contribution of magmatic and hydrothermal processes to rare metal enrichment has been a key issue for the alkaline-associated rare metal deposits. Till now, our understanding on the rare metal concentration of extrusive peralkaline magmatic systems is rather limited. We try to address this issue by studying the Tudiling trachyte Nb-Ta-Zr-REE deposit in the South Qinling (SQ), which is well endowed with abundant alkaline-associated rare metal deposits. Four lithofacies (i.e., trachyte, trachytic tuff, trachytic phyllite and trachytic ignimbrite) with rare metal mineralization were thoroughly investigated on their emplacement ages, whole-rock geochemistry, and Nb-REE mineralogy to decipher the evolution of the system and the concentration mechanisms for the rare metals. Zircon U-Pb dating indicates that the former three lithofacies developed during the Early Silurian (445–442 Ma) and are coeval with their intrusive counterparts, i.e., the Miaoya and Shaxiongdong syenites in the SQ. They share similar element distribution patterns (Nb-Ta, Zr-Hf, LREE enrichments, and Sr, P, Ti depletions) and moderately depleted Nd isotopes (εNd(t) values: 2.3–3.1), indicating a common mantle source. In contrast, the trachytic ignimbrite erupted during the late Jurassic (157 ± 1.9 Ma) and has enriched Nd isotope compositions (εNd(t) values: −2.9–−2.8), implying an enriched mantle source, which had probably been modified by the residuals of the Mianlue oceanic sediments. Their bulk-rock rare metal concentrations indicate that the former three lithofacies are characterized by Nb-Ta-Zr mineralization/enrichment with the phyllite containing the highest grades, while the latter one has REE mineralization as well as Nb-Ta-Zr mineralization/enrichment. Our geochemical and mineralogical results suggested that rare metal enrichment in these trachytic rocks was initially attributed to the partial melting of an enriched mantle source and subsequent protracted fractional crystallization of alkaline basaltic magmas. Effects of late-stage hydrothermal alteration on rare metal upgrading are highly dependent on rock structures and distinct on the intensively altered phyllite and ignimbrite.

1. Introduction

Rare metals have critical uses in the modern industrial development and are increasingly required for a variety of technological applications, such as medical instrumentation, defensive systems, alloys, and electronics (e.g., Chakhmouradian and Wall, 2012). Nevertheless, the global supply for rare metals is currently limited (e.g., Weng et al., 2015). To alleviate the supply–demand contradiction, prospecting new rare metal deposits is urgent. It is well recognized that majority of rare metal deposits worldwide have affinity with carbonatites and intrusive alkaline and peralkaline rocks (i.e., syenite, peralkaline granite and pegmatite) (Chakhmouradian and Zaitsev, 2012), which have been the major targets for rare metal exploration. Till now, our understanding on the mechanism of the rare metal mineralization in these systems is rather

* Corresponding author at: CAS Key Laboratory of Mineralogy and Metallogeny/Guangdong Provincial Key Laboratory of Mineral Physics and Materials, Guangzhou Institute of Geochemistry, Chinese Academy of Sciences, Guangzhou 510640, China.
E-mail address: qshan@gig.ac.cn (Q. Shan).

https://doi.org/10.1016/j.oregeorev.2021.104535
Received 22 April 2021; Received in revised form 10 October 2021; Accepted 18 October 2021
Available online 25 October 2021

limited. Due to the incompatibility of rare metals during most magmatic evolution, their enrichment can be initially attributed to protracted fractional crystallization (e.g., Chakhmouradian and Zaitsev, 2012; Chandler and Spandler, 2020; Schmitt et al., 2002; Spandler and Morris, 2016) and low-degree melting of enriched mantle sources (e.g., Chakhmouradian and Wall, 2012). Other processes, like liquid immiscibility (e.g., Spandler and Morris, 2016; Thomas et al., 2006; Williams-Jones and Migdisov, 2014; Williams-Jones et al., 2012), magmatic crystal accumulation (e.g., Sheard et al., 2012), hydrothermal metasomatism (e.g., Dostal et al., 2014; Salvi and WilliamsJones, 1996; Williams-Jones et al., 2012), and weathering (e.g., Chakhmouradian and Wall, 2012; Li et al., 2020), may have upgraded rare metal concentrations. However, for the peralkaline magmatic systems of different locations, the leading processes that promote the rare metal mineralization are variable and highly dependent on their rock compositions and occurrences.

While most peralkaline rocks with rare metal mineralization are intrusive, there are some notable examples of extrusive peralkaline rare metal deposits, such as the Toongi deposit (Spandler and Morris, 2016), the Brockmans deposit (Ramsden et al., 1993; Taylor et al., 1995a; b), and the Peak Range deposit (Chandler and Spandler, 2020) in Australia, the Foxtrot deposit in Canada (Miller, 2015), and the Round Top deposit in America (Pingitore et al., 2014). The former two deposits are mainly associated with peralkaline trachytes while the latter three are related to peralkaline rhyolites. Compared with intrusive peralkaline rocks, these extrusive counterparts were emplaced at shallow depth and experienced rapid cooling to generate volcanic textures, and thus preserved the primary magmatic textures and mineral compositions of peralkaline magmas (e.g., Spandler and Morris, 2016). Previous studies suggested that the contribution of magmatic and hydrothermal processes to rare metal enrichment shows some variations between different extrusive peralkaline magmatic systems. For instance, the rare metal mineralization at Toongi was suggested to have resulted from protracted fractional crystallization of the alkaline magmas under low fO_2 and H_2O-activity conditions and subsequent liquid immiscibility (Spandler and Morris, 2016). The mineralization at Brockmans was predominantly controlled by the alteration of the magmatic precursor minerals, i.e., zircon and columbite, and the resultant rare metal remobilization by fluorine-rich deuteric fluids (Ramsden et al., 1993). As for the Peak Range, Foxtrot and Round Top deposits, their concentrations of rare metal to the economic grades represented the combined products of protracted fractional crystallization of alkaline magmas and subsequent hydrothermal alteration and weathering (Chandler and Spandler, 2020; Miller, 2015; Pingitore et al., 2014).

The South Qinling (SQ) has become a potential metallogenic belt for rare metal resources since the discovery of the large-scale Miaoya (MY) syenite-carbonatite Nb-REE deposit in 1980s (Li, 1980). Subsequently, several medium-to-large-scale alkaline-associated rare metal deposits, including the Shaxiongdong (SXD) syenite-carbonatite Nb-REE deposit, and the Tudiling, Tianbao, Zhujiayuan, Shuanghekou and Haoping trachyte Nb(-Ta-Zr-REE) deposits, were successively found in the Wudang Uplift and the North Daba Mountains, making the SQ one of the most important rare metal metallogenic belts in China. Previous studies on the rare metal deposits of the SQ mainly focused on the rare metal mineralization related to syenites, like the MY deposit (e.g., Çimen et al., 2018; Li, 1980; Qiu et al., 2017; Su et al., 2019; Xu et al., 2010, 2015, Ying et al., 2017, 2020; Zhang et al., 2019a; Zhu et al., 2017; Zhang et al., 2019b), and the SXD deposit (e.g., Chen et al., 2018; Xu et al., 2008; Zhang et al., 2019b), while investigations on these trachyte associated cases in the SQ were relatively limited (e.g., Nie et al., 2020; Xiong et al., 2018; Yang et al., 2017). To reveal the relative contribution of magmatic and hydrothermal processes to the rare metal concentration in the extrusive peralkaline magmatic systems, this study focuses on the newly-discovered large-scale Tudiling trachyte Nb-Ta-Zr-REE deposit, and investigates the timing, petrogenesis, and source nature of the four ore-bearing trachytic lithofacies, and mineralogy and textures of Nb-REE minerals to reveal their rare metal concentration mechanisms. These results would be crucial to deciphering the rare metal mineralization of the Tudiling deposit and add fresh information for understanding the rare metal concentration in the extrusive peralkaline magmatic systems.

2. Regional geology

The Qinling orogen is part of the Central China Orogenic Belt and sandwiched between the North China Craton to the south and the South China Block (SCB) to the north (Fig. 1A). Tectonically, the SQ is separated from the North Qinling (NQ) and the SCB by the Shangdan and Mianlue suture zones, respectively (Fig. 1B). During the Early Devonian, the northward subducted Shangdan Ocean closed, leading to the assemblage of the NQ and the SCB (Dong et al., 2011; Dong and Santosh, 2016). The Mianlue Ocean opened up through an intraplate rifting during the middle Devonian and continued to expand until the Carboniferous, separating the SQ from the northern margin of the SCB as an independent micro-plate (Zhang et al., 2001; 2004). From the Permian to the Early Triassic, the Mianlue Ocean subducted northwards beneath the SQ and became extinct during the middle-to-late Triassic, triggering the collision between the SQ and the SCB (Dong et al., 2011; Dong and Santosh, 2016). In the Early Jurassic, the SQ and NQ conversed into post-collision collapse, accompanied by the formation of fault-bounded basins in the uplifted area of the Mianlue suture zone and the SQ (Dong et al., 2011; Meng and Zhang, 2000).

The SQ possesses a Precambrian basement, unconformably covered by the Sinian to Mesozoic sedimentary rocks and intruded by the Silurian syenites and carbonatites, and the Triassic to the Early Cretaceous granitoids (Dong et al., 2008, 2011; Dong and Santosh, 2016; Zhang et al., 2001) (Fig. 1B). The Proterozoic basement complexes mainly consist of the Paleoproterozoic plutonometamorphic rocks and the Meso-to-Neoproterozoic volcanic-sedimentary assemblages (Ling et al., 2008; Zhang et al., 2000, 2001). The cover rocks include the Neoproterozoic clastic and carbonate rocks, Cambrian-Ordovician limestones, Silurian shales, Devonian-Carboniferous clastic rocks, and a few Permian-Lower Triassic sandstones (Zhang et al., 2001).

3. Deposit geology and samples

3.1. Deposit geology

The Tudiling trachyte Nb-Ta-Zr-REE deposit is located in the southwestern margin of the Wudang Uplift of the SQ. The strata in the deposit include the mid-late Proterozoic (Nanhua Period) Yaolinghe and Wudang Groups, the Sinian Jiangxigou and Huohua Formations, the Cambrian Yangjiabao, Zhuangzigou and Zhushan Formations, the Silurian Meiziya Formation and Quaternary (Fig. 2). The Proterozoic strata are composed of metavolcanic rocks and metasedimentary rocks, and the Sinian strata consist of clastic rocks and carbonate rocks, and the Cambrian strata contain limestone, slate and phyllite. The Silurian Meiziya Formation is the major ore-hosting strata and contains abundant trachytic rocks and metamafic rocks hosted by the argillaceous and silt slate (Fig. 2) (according to the Nb-Au investigation and evaluation report of the Zhushan-Zhuxi region in Hubei).

The magmatic rocks in the mining zone are predominantly trachytic rocks with lesser metadiabase/metagabbro and orthophyre in its southwestern part (Fig. 2). The trachytic rocks are closely associated with Nb-Ta-Zr-REE mineralization and are the major host rocks of ore metals. The distribution of these trachytic rocks is mainly controlled by fractures of the east–west and north–north-west directions. Till now, a total of eight orebodies have been identified in the mining zone and occur as layered and lenticular beds within the trachytic rocks. Most orebodies are distributed along the bedding of the strata and the trachytic rocks with rare metal mineralization have four lithofacies, i.e., trachyte (subvolcanic lithofacies, orebody III and V), trachytic

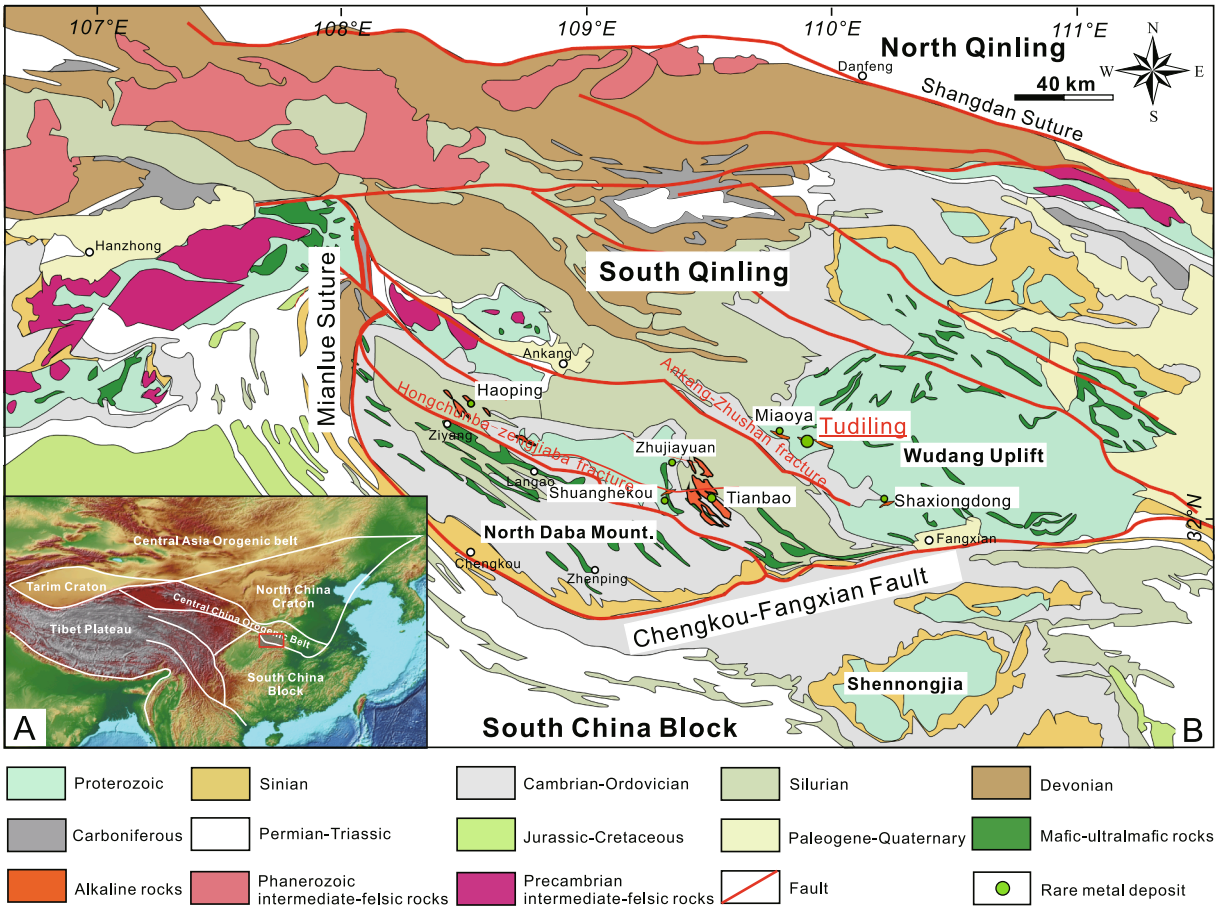

Fig. 1. (A) Topography of China and adjacent regions, showing the major tectonic units and location of South Qinling (red box); (B) Geological map of South Qinling, showing the locations of Tudiling Nb-Ta-Zr-REE deposits and the other rare metal deposits in the South Qinling, modified after Wang et al. (2017). (For interpretation of the references to colour in this figure legend, the reader is referred to the web version of this article.)

ignimbrite (overflowing facies, orebody II and VIII), trachytic tuff (eruptive facies, orebody VI) and trachytic phyllite (*meta*-sedimentary facies, orebody I, IV and VII) (Fig. 2).

3.2. Samples and petrography

Representative samples of the four trachytic lithofacies (eight trachyte samples (19NG-01 to -09), eight trachytic tuff samples (19TD-01 to -08), four trachytic phyllite samples (19TD-18 to -21) and four trachytic ignimbrite samples (19TD-22 to -26)) were collected from the orebodies I, II, III, and VI (sampling locations shown in Fig. 2), respectively. All the trachytic lithofacies have experienced hydrothermal alteration to variable extents. Their petrographic observations are described as follows:

Trachyte is of porphyritic texture and massive structure (Fig. 3A). The phenocrysts are predominantly orthoclase (10 vol%) and albite (5 vol%), which are euhedral tabular in shape and 0.5–2.0 mm in size. The matrix consists of albite (40 vol%), sericite (40 vol%), ilmenite (3 vol%), and limonite (3 vol%) (Fig. 3B). Albite in matrix is xenomorphic and < 0.05 mm in size. Sericite is scaly and represents the alteration of orthoclase and albite. Limonite is mainly distributed along albite phenocryst margins.

Trachytic tuff is of pyroclastic texture and massive structure, and consists of albite (50 vol%), orthoclase (20 vol%), sericite (20 vol%) and minor biotite, ilmenite and limonite. Orthoclase pyroclasts are subhedral tabular in shape and ~ 0.2 mm in size (Fig. 3C). Albite pyroclasts are anhedral and <0.05 mm in size (Fig. 3D). Sericite is scaly in shape and mostly clusters as groups and may represent tephra recrystallization (Fig. 3D).

Trachytic phyllite is of microgranular crystalloblastic texture and phyllitic structure (Fig. 3E). It is mainly composed of sericite (50 vol%) and albite (37 vol%) with minor quartz (5 vol%), Fe-sulfate (3 vol%) and limonite (3 vol%) (Fig. 3F). Sericite displays oriented arrangement along microfold structures due to metamorphic stress (Fig. 3F). Albite crystals are subhedral-to-euhedral in shape and vary from 0.05 to 2 mm in size. Quartz grains are granular and occur as crystalloblasts, while Fe-sulfates and hematite are distributed along the micro-fractures.

Trachytic ignimbrite is of tuffaceous texture and flow structure, and consists of crystal pyroclasts (85 vol%) and cements (10 vol%) (Fig. 3G). Crystal pyroclasts are predominantly albite and sericite, which are subangular and 0.05–0.5 mm in size (Fig. 3H). The cements are mainly composed of Fe-Mn oxides, albite and sericite.

Though the four trachytic lithofacies exhibit distinct textures and structures, they share common ore mineral phases, i.e., the Zr-rich mineral (zircon), Nb-rich minerals (columbite and ilmenorutile) and REE-rich minerals (apatite, monazite, allanite and bastnaesite) (Fig. 4). Scanning electron microscope (SEM) observations suggest that the trachytic ignimbrite has more REE-rich minerals than the other three lithofacies, consistent with their higher REE concentrations (illustrated in a later section). Zircon is the major Zr-bearing mineral phase, and displays two occurrences, i.e., zircon clusters (Fig. 4A) and anhedral zircon grains (Fig. 4E and H). Columbite and ilmenorutile predominate the Nb-rich mineral phases. Columbite usually displays metasomatism relationship with ilmenite and ilmenorutile (Fig. 4C and D). Sometimes, it shows well intergrowth with monazite (Fig. 4B and C). Ilmenorutile also has two occurrences, i.e., metasomatic product of ilmenite (Fig. 4C)

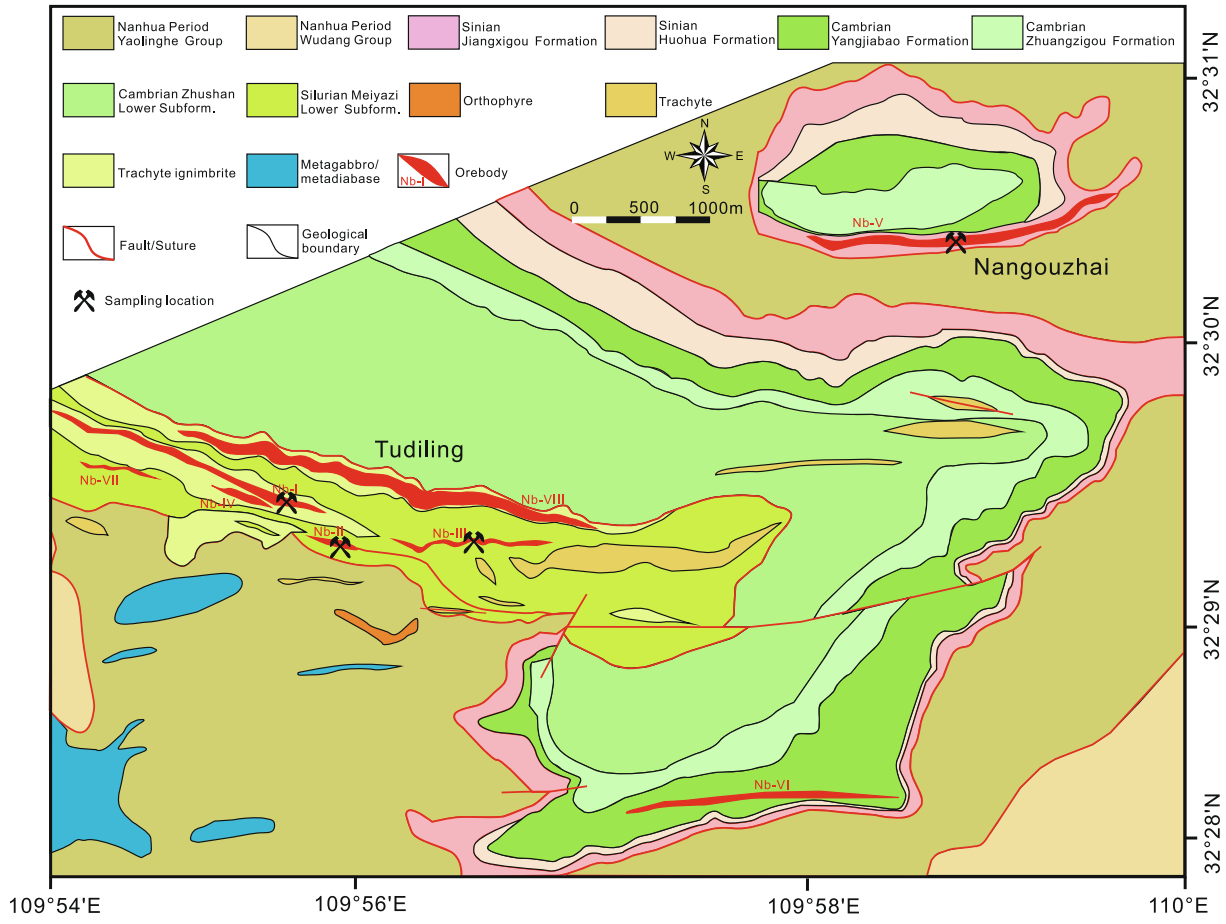

Fig. 2. Geological map of the Tudiling trachyte Nb-Ta-Zr-REE deposits with the eight orebodies marked (modified after Xiong et al. (2018)), showing the sampling locations of the four trachytic lithofacies.

and disseminated anhedral grains (Fig. 4D). REE-rich mineral phases include apatite, monazite, allanite, and bastnaesite. Apatite is of large size (50–200 μm) and shows as an anhedral grain (Fig. 4F). Monazite is mostly fine-grained and has three occurrences, i.e., intergrown with columbite (Fig. 4B and C), scattered monazite grains (Fig. 4F) and monazite clusters (Fig. 4G). Allanite and bastnaesite represent metasomatic products of the augite in Fig. 4H, and some allanite show intergrowth relationship with albite (Fig. 4I).

4. Analytical methods

4.1. Whole-rock geochemical analyses

Whole-rock samples were firstly examined using optical microscopy. Representative samples were selected and crushed into 200-mesh powder for geochemical analyses. The major and trace elements are analyzed at the State Key Laboratory of Isotope Geochemistry, Guangzhou institute of geochemistry, Chinese Academy of Sciences (GIGCAS). Major elements were determined using the standard X-ray fluorescence (XRF, Rigaku RIX 2100) method, with analytical precision better than 4%. Trace elements were analyzed using a Thermo Fisher iCAP RQ inductively coupled plasma mass spectrometry (ICP-MS). Analytical precision for most elements is better than 5%.

To track the source signatures of the Tudiling trachytic rocks, whole-rock Sm–Nd isotopic analyses of selected samples were determined. Sample powders were first dissolved in Teflon capsules with HF + HNO_3 acid. Secondly, REEs were separated using cation columns, and then Nd fractions were further separated using HDEHP-coated columns. Nd isotopic compositions were analyzed on the Neptune Plus multi-collector mass spectrometer at GIGCAS, following procedures similar to those of Wei et al. (2002) and Liang et al. (2003). Measured $^{143}Nd/^{144}Nd$ ratios were normalized to $^{146}Nd/^{144}Nd = 0.7219$. The $^{143}Nd/^{144}Nd$ ratio of the Standard Shin Etsu JNdi-1 determined during this study was 0.512115 ± 0.000010 (2SD).

4.2. Zircon in-situ U-Pb isotopic analyses

Representative samples were selected from each of the four trachytic lithofacies. Zircon grains were separated through crushing rock samples to about 80 mesh powder, desliming in water, followed by density separation, magnetic separation and handpicking, then mounted in epoxy and polished to nearly a half section to expose internal structures. Cathodoluminescence (CL) and optical microscopy images of zircon grains were obtained in order to ensure that the least fractured, inclusion-free zones in zircon were analyzed. Zircon U–Pb dating was undertaken by using the laser ablation inductively coupled plasma spectrometry (LA-ICPMS) (Resonetics Resolution S-155 laser *plus* Agilent 7900), at the CAS Key Laboratory of Mineralogy and Metallogeny, GIGCAS. NIST SRM 610 glass (Pearce et al., 1997), zircon 91500 standard (Wiedenbeck et al., 1995), and Plesovice zircon standards (Slama et al., 2008) were used as external standards. All analyses were carried out at a laser energy of 60 mJ, with a beam diameter of 29 μm and a repetition rate of 6 Hz. Integration of background and analytical signals, and time-drift correction and quantitative calibration for trace elements and U-Pb isotopes, were undertaken by using the software Iolite_*v4.2* (Paton et al., 2011). Concordia diagrams and weighted mean calculations were made using *Isoplot_v3.75* program (Ludwig, 2012).

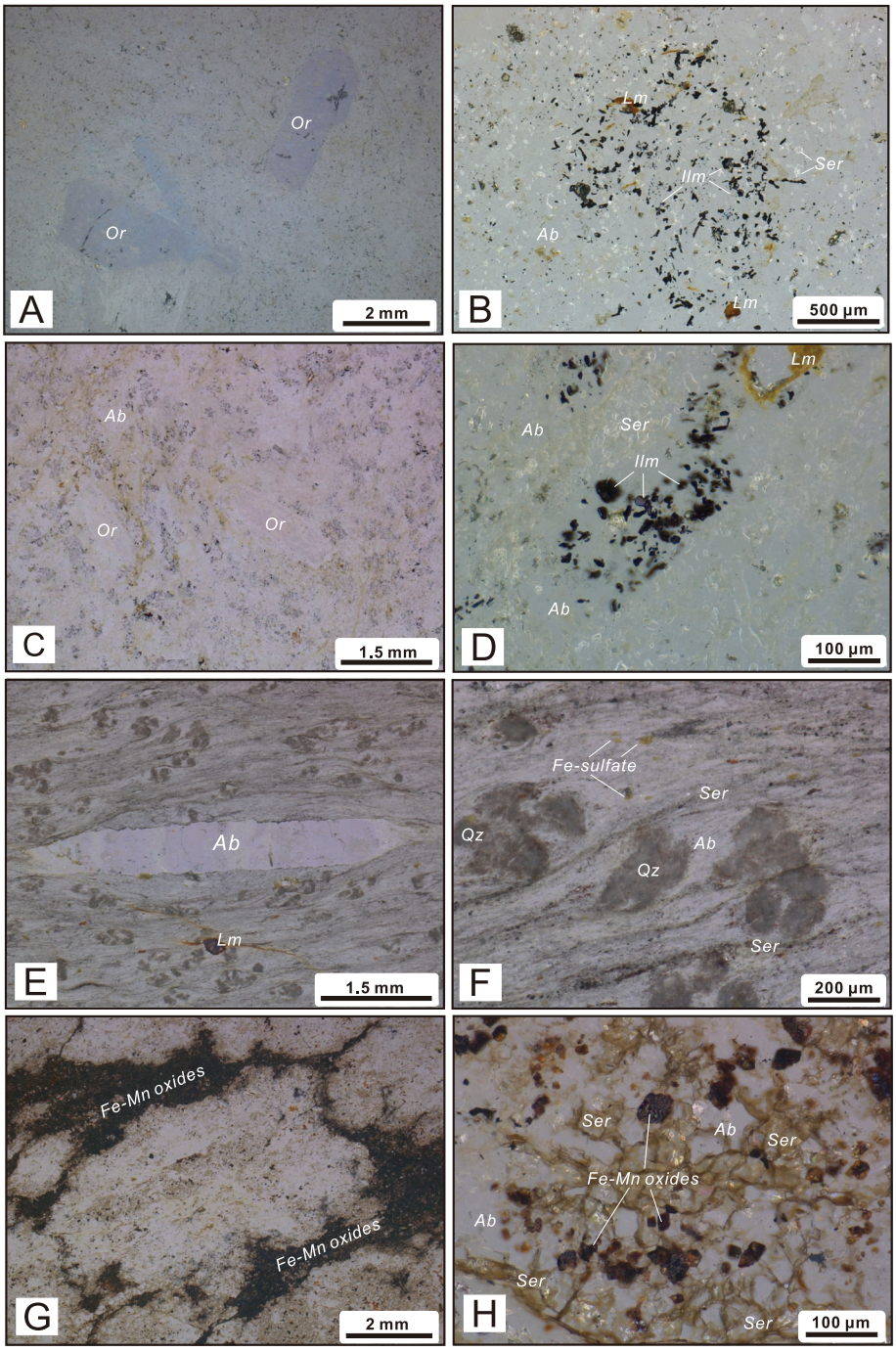

Fig. 3. Petrographic observations of the (A–B) trachyte, (C–D) trachytic tuff, (E–F) trachytic phyllite and (G–H) trachytic ignimbrite from the Tudiling, South Qinling. Mineral abbreviations: *Or* orthoclase, *Ab* albite, *Ser* sericite, *Ilm* ilmenite, *Lm* limonite, *Qz* quartz.

4.3. SEM observation and energy dispersive spectrometer (EDS) analyses

Carbon-coated thin sections of representative samples were used for SEM observation and mineral phase identification. These analyses were done with the Phenom TM scanning electron microscope at the CAS Key Laboratory of Mineralogy and Metallogeny, GIGCAS. Backscattered electron images (BSE) of interested areas were taken under 15 kV and image mode. EDS analyses of interested points were done with a 3-μm defocused beam under 15 kV and point analysis mode. The EDS analysis results are provided in the Supplementary Materials.

5. Results

5.1. Zircon U–Pb dating

Zircon U–Pb data for the four trachytic lithofacies are presented in Table 1 and plotted in Fig. 5, and zircon crystal features and dating results are described as follows.

Zircon crystals from the trachyte (sample 19NG-03) are transparent and light brown with irregular shapes, and show evident oscillatory magmatic zonings without inherited cores on their CL images (Fig. 5A). The zircon crystals are of large size (50–200 μm) for the crystal long axis. Their U and Th contents are 452144 ppm (551 ppm on average) and

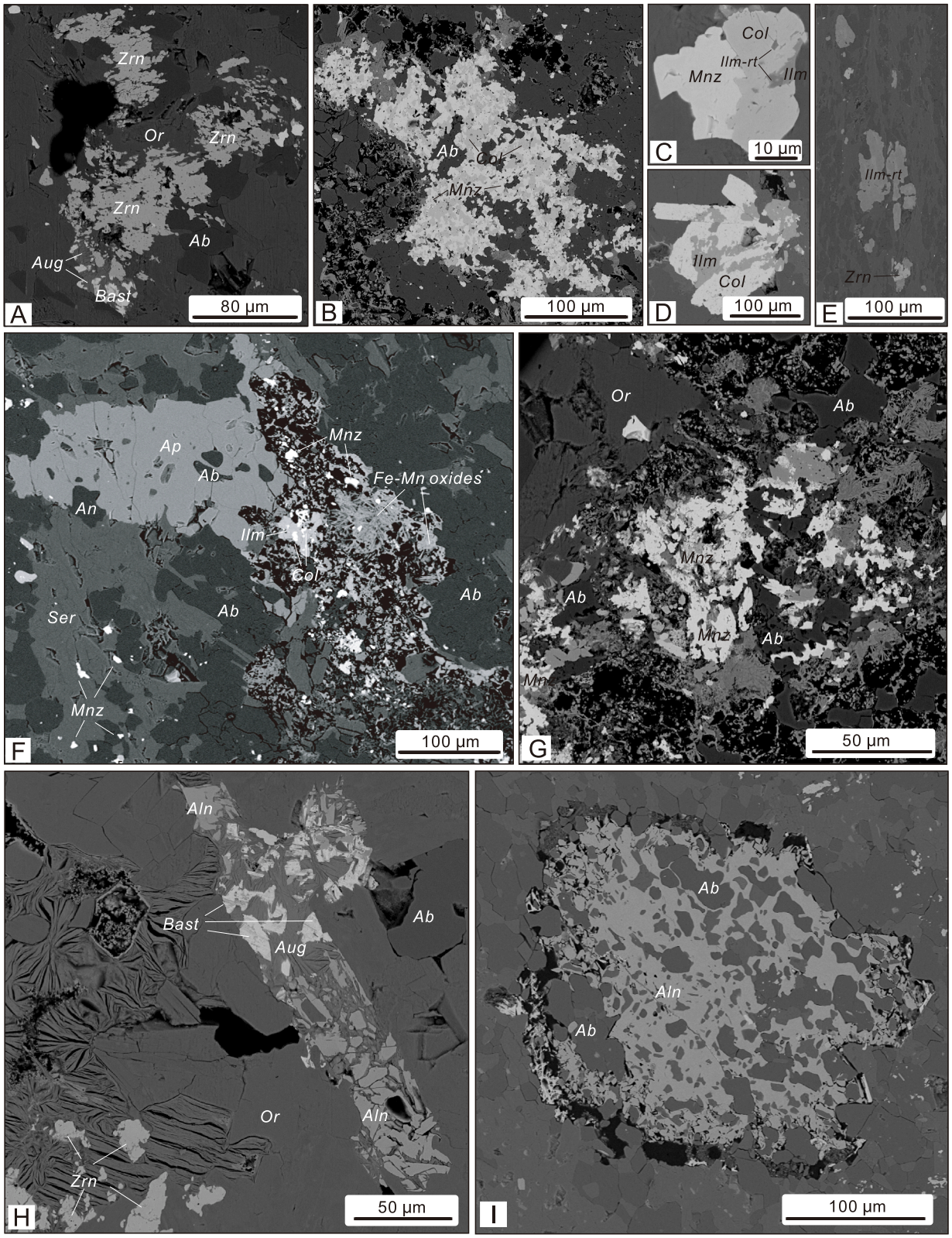

Fig. 4. Backscattered electron (BSE) images of major Nb-REE minerals from the Tudiling trachytic rocks, showing their occurrences and spatial relationship with adjacent minerals. Their corresponding EDS analysis results are provided in the Supplementary materials. Mineral abbreviations: *Ab* albite, *Aln* allanite, *An* anorthite, *Ap* apatite, *Aug* augite, *Bast* bastnaesite, *Col* columbite, *Ilm* ilmenite, *Ilm-rt* ilmenorutile, *Mnz* monazite, *Or* orthoclase, *Ser* sericite, *Zrn* zircon.

Table 1
Laser ablation ICP-MS zircon U–Pb data of the Tudiling trachytic rocks.

Sample	Concentrations and ratios				Isotope ratios					Apparent ages (Ma)			
	U (ppm)	Th (ppm)	Th/U ratio	Pb (ppm)	$^{206}Pb/^{238}U$ ratio	2SE	$^{207}Pb/^{235}U$ ratio	2SE	rho	$^{206}Pb/^{238}U$ age	2SE	$^{207}Pb/^{235}U$ age	2SE
19NG-03 (Trachyte)													
19NG-03-01	410	233	0.57	27.91	0.071	0.002	0.548	0.019	0.26	441	9	441	12
19NG-03-02	654	944	1.44	56.25	0.072	0.002	0.556	0.015	0.20	446	9	447	10
19NG-03-03	483	462	0.96	32.35	0.072	0.002	0.529	0.022	0.23	450	10	428	15
19NG-03-04	376	210	0.56	26.06	0.071	0.002	0.557	0.020	0.26	441	9	446	13
19NG-03-05	560	346	0.62	39.66	0.072	0.002	0.556	0.014	0.19	447	9	447	9
19NG-03-06	514	399	0.78	36.50	0.072	0.002	0.545	0.017	0.25	450	9	440	11
19NG-03-07	348	325	0.93	22.35	0.072	0.002	0.551	0.022	0.33	449	10	446	15
19NG-03-08	818	1171	1.43	70.76	0.072	0.002	0.560	0.013	0.36	450	9	451	8
19NG-03-09	85	1246	14.74	26.66	0.071	0.002	0.567	0.034	0.05	442	12	450	23
19NG-03-11	250	173	0.69	18.16	0.071	0.002	0.560	0.022	0.10	441	10	448	15
19NG-03-12	118	54	0.45	10.21	0.072	0.002	0.572	0.038	0.06	449	12	453	25
19NG-03-13	291	161	0.55	20.84	0.072	0.002	0.576	0.022	0.28	448	10	459	14
19NG-03-14	1883	3539	1.88	173.0	0.074	0.002	0.571	0.013	0.52	459	9	457	9
19NG-03-15	67	1347	20.07	26.37	0.070	0.002	0.559	0.044	0.04	439	13	444	30
19NG-03-16	332	228	0.69	23.76	0.072	0.002	0.549	0.020	0.17	448	10	442	13
19NG-03-17	908	1165	1.28	64.06	0.072	0.002	0.558	0.016	0.45	448	10	449	11
19NG-03-18	381	214	0.56	26.45	0.070	0.002	0.553	0.017	0.19	438	9	445	11
19NG-03-21	191	263	1.37	17.59	0.070	0.002	0.538	0.024	0.03	436	10	432	16
19NG-03-22	2144	4070	1.90	206.9	0.074	0.002	0.584	0.011	0.38	461	9	466	7
19NG-03-23	632	675	1.07	50.51	0.072	0.002	0.553	0.014	0.15	446	9	446	9
19NG-03-24	755	1057	1.40	65.31	0.071	0.001	0.558	0.014	0.37	441	9	449	9
19NG-03-25	532	613	1.15	42.07	0.071	0.002	0.553	0.016	0.34	445	9	448	11
19NG-03-26	869	716	0.82	65.64	0.071	0.002	0.547	0.015	0.27	439	9	442	10
19NG-03-27	310	217	0.70	23.14	0.071	0.002	0.565	0.020	0.05	444	10	452	13
19NG-03-28	45	17	0.37	3.78	0.070	0.002	0.564	0.053	0.07	437	14	437	34
19NG-03-29	596	631	1.06	50.09	0.071	0.002	0.558	0.016	0.27	442	9	449	10
19NG-03-30	645	618	0.96	50.23	0.071	0.002	0.576	0.015	0.18	444	9	461	10
19NG-03-31	439	377	0.86	34.20	0.070	0.002	0.558	0.017	0.24	437	9	449	11
19NG-03-32	143	93	0.65	10.62	0.072	0.002	0.534	0.031	0.00	448	11	429	20
19NG-03-33	515	459	0.89	43.80	0.072	0.002	0.572	0.016	0.22	447	9	457	10
19NG-03-34	218	133	0.61	18.73	0.072	0.002	0.576	0.021	0.11	450	10	459	14
19NG-03-35	1205	1341	1.11	89.79	0.072	0.002	0.552	0.015	0.31	447	9	446	10
19NG-03-36	401	290	0.72	30.42	0.072	0.002	0.570	0.017	0.19	447	10	457	12
19NG-03-37	623	675	1.08	42.82	0.073	0.002	0.539	0.022	0.44	456	12	437	15

(*continued on next page*)

Table 1 (*continued*)

Sample	Concentrations and ratios				Isotope ratios					Apparent ages (Ma)			
	U (ppm)	Th (ppm)	Th/U ratio	Pb (ppm)	$^{206}Pb/^{238}U$ ratio	2SE	$^{207}Pb/^{235}U$ ratio	2SE	rho	$^{206}Pb/^{238}U$ age	2SE	$^{207}Pb/^{235}U$ age	2SE
19TD-03 (Trachytic tuff)													
19TD-03-01	51	126	2.46	4.61	0.071	0.002	0.557	0.056	0.22	440	12	430	36
19TD-03-02	750	664	0.89	44.50	0.072	0.001	0.563	0.030	0.26	448	6	452	19
19TD-03-03	254	136	0.53	16.81	0.070	0.001	0.534	0.031	0.11	436	7	433	21
19TD-03-04	263	2162	8.23	40.92	0.070	0.002	0.552	0.036	0.19	440	8	444	24
19TD-03-05	351	196	0.56	18.87	0.072	0.001	0.556	0.036	0.01	449	8	446	24
19TD-03-06	717	2528	3.52	104.85	0.070	0.001	0.565	0.027	0.27	439	6	455	18
19TD-03-07	424	387	0.91	31.30	0.071	0.001	0.560	0.028	0.19	442	6	449	18
19TD-03-08	328	301	0.92	24.25	0.071	0.001	0.565	0.029	0.04	444	6	452	19
19TD-03-09	236	200	0.85	20.94	0.070	0.001	0.534	0.032	0.01	438	8	432	21
19TD-03-10	505	343	0.68	25.00	0.072	0.003	0.533	0.035	0.55	450	16	431	23
19TD-03-11	858	185	0.22	45.19	0.070	0.001	0.531	0.026	0.10	437	6	433	17
19TD-03-12	556	568	1.02	41.59	0.071	0.002	0.532	0.028	0.27	443	9	432	19
19TD-03-13	468	1913	4.09	59.05	0.071	0.002	0.534	0.030	0.40	443	10	432	20
19TD-03-14	493	2395	4.86	69.77	0.071	0.002	0.562	0.030	0.31	444	9	451	20
19TD-03-15	273	205	0.75	25.58	0.074	0.002	0.571	0.038	0.07	462	10	456	25
19TD-03-16	597	985	1.65	66.31	0.075	0.002	0.572	0.035	0.55	468	12	457	23
19TD-03-17	844	1406	1.67	75.57	0.073	0.002	0.548	0.029	0.52	453	10	445	20
19TD-03-18	280	151	0.54	21.72	0.071	0.001	0.539	0.033	0.19	442	9	435	22
19TD-03-19	286	124	0.43	22.31	0.073	0.002	0.553	0.035	0.05	453	9	445	23
19TD-03-20	533	112	0.21	26.37	0.071	0.002	0.561	0.039	0.61	443	14	446	23
19TD-18 (Trachytic phyllite)													
19TD-18-01	18	23	1.27	1.45	0.071	0.003	0.528	0.084	0.16	442	14	388	55
19TD-18-02	53	1742	32.62	23.86	0.071	0.003	0.598	0.078	0.14	442	15	459	48
19TD-18-03	54	19	0.34	3.94	0.071	0.003	0.567	0.047	0.16	441	16	444	31
19TD-18-04	58	42	0.73	4.31	0.071	0.002	0.557	0.053	0.04	444	14	438	35
19TD-18-05	73	1588	21.85	25.03	0.071	0.002	0.604	0.060	0.19	445	14	467	38
19TD-18-06	498	3944	7.92	82.06	0.072	0.001	0.547	0.018	0.21	445	9	441	12
19TD-18-07	607	696	1.15	51.19	0.072	0.001	0.548	0.016	0.47	446	8	442	10
19TD-18-08	688	857	1.25	51.65	0.071	0.001	0.569	0.018	0.20	441	7	455	12
19TD-25 (Trachytic ignimbrite)													
19TD-25-01	639	311	0.49	14.45	0.0242	0.0005	0.168	0.010	0.01	154	3	157	8
19TD-25-02	2062	520	0.25	44.01	0.0249	0.0003	0.171	0.004	0.28	158	2	160	4
19TD-25-03	955	514	0.54	18.36	0.0244	0.0007	0.178	0.012	0.44	156	4	166	10
19TD-25-04	807	222	0.28	21.07	0.0242	0.0004	0.177	0.011	0.29	154	2	165	9
19TD-25-05	988	402	0.41	26.50	0.0245	0.0007	0.166	0.012	0.39	156	4	156	10
19TD-25-06	803	561	0.70	17.68	0.0252	0.0006	0.173	0.007	0.34	161	4	161	6
19TD-25-07	832	468	0.56	18.53	0.0250	0.0005	0.177	0.009	0.23	159	3	165	7

(*continued on next page*)

Table 1 (*continued*)

Sample	Concentrations and ratios				Isotope ratios					Apparent ages (Ma)			
	U (ppm)	Th (ppm)	Th/U ratio	Pb (ppm)	$^{206}Pb/^{238}U$ ratio	2SE	$^{207}Pb/^{235}U$ ratio	2SE	rho	$^{206}Pb/^{238}U$ age	2SE	$^{207}Pb/^{235}U$ age	2SE
19TD-25-08	886	494	0.56	19.66	0.0253	0.0005	0.171	0.007	0.25	161	3	160	6
19TD-25-09	702	456	0.65	16.01	0.0249	0.0007	0.169	0.008	0.36	158	4	158	7
19TD-25-10	705	471	0.67	21.23	0.0238	0.0004	0.168	0.008	0.33	151	2	157	7
19TD-25-11	1033	525	0.51	19.45	0.0247	0.0006	0.178	0.010	0.27	157	4	166	9
19TD-25-12	668	518	0.77	12.01	0.0250	0.0005	0.177	0.009	0.30	159	3	165	8
19TD-25-13	867	473	0.55	21.48	0.0235	0.0005	0.162	0.014	0.00	150	3	151	12
19TD-25-14	413	243	0.59	12.47	0.0249	0.0007	0.181	0.013	0.05	158	4	169	11
19TD-25-15	598	337	0.56	12.86	0.0253	0.0006	0.189	0.010	0.01	161	4	175	9
19TD-25-16	838	478	0.57	20.77	0.0250	0.0009	0.182	0.010	0.15	159	5	169	9

54–4070 ppm (719 ppm on average), respectively. Their Th/U ratios range from 0.37 to 20.07, mostly consistent with those (> 0.4) of the magmatic zircon (>0.4). Thirty-three U–Pb analyses of zircon grains yield a concordant U–Pb age of 446 ± 2 Ma, MSWD = 0.9 (Fig. 5B). Their $^{206}Pb/^{238}U$ ages range from 436 Ma to 461 Ma and return a weighted mean age of 445 ± 2 Ma, MSWD = 0.9 (Fig. 5C).

Zircon crystals from the trachytic tuff (sample 19TD-03) have similar appearance with those from the trachyte (Fig. 5D). Their U and Th contents are 51 – 858 ppm (453 ppm on average) and 112 – 2528 ppm (754 ppm on average), respectively. Their Th/U ratios range from 0.21 to 8.23. Nineteen U–Pb analyses of zircon grains yield a concordant U–Pb age of 441 ± 2 Ma, MSWD = 1.8 (Fig. 5E). Their $^{206}Pb/^{238}U$ ages range from 436 Ma to 453 Ma and yield a weighted mean age of 442 ± 3 Ma, MSWD = 1.9 (Fig. 5F).

Zircon crystals in the trachytic phyllite (sample 19TD-18) are also of irregular shape with evident oscillatory magmatic zonings (Fig. 5G), similar to those in the trachyte and trachytic tuff. Their U and Th contents are 18–688 ppm (256 ppm on average) and 193944 ppm (1114 ppm on average), respectively and their Th/U ratios range from 0.34 to 32.62, mostly consistent with those of the magmatic zircon (>0.4). Eight U–Pb analyses of zircon grains yield a concordant U–Pb age of 446 ± 3 Ma, MSWD = 1.1 (Fig. 5H). Their $^{206}Pb/^{238}U$ ages range from 441 Ma to 446 Ma and yield a weighted mean age of 445 ± 4 Ma, MSWD = 0.6 (Fig. 5I).

Zircon crystals from the trachytic ignimbrite (sample 19TD-25) are subhedral-to-euhedral in shape and small in size with 40–60 μm for the crystal long axis, showing evident oscillatory magmatic zonings (Fig. 5J). Their U and Th contents are 413–2062 ppm (862 ppm on average) and 222–561 ppm (437 ppm on average), respectively and their Th/U ratios range from 0.25 to 0.77. Fifteen U–Pb analyses of zircon grains yield a concordant U–Pb age of 157 ± 3 Ma, MSWD = 3.4 (Fig. 5K). Their $^{206}Pb/^{238}U$ ages range from 151 Ma to 161 Ma and return a weighted mean age of 157 ± 1.9 Ma, MSWD = 4.7 (Fig. 5L).

Above all, the trachyte, tuff and phyllite have consistent zircon U–Pb ages and developed during the early Silurian (445–442 Ma), while the trachytic ignimbrite yields a zircon U–Pb age of 157 ± 1.9 Ma and formed during the late Jurassic period. Additionlly, the Silurian zircons exhibit different REE distribution patterns from those of the Jurassic ones (Fig. 6A and Supplementary Table S1), with the latter possessing obvious negative Eu anomalies (Eu/Eu*: 0.10–0.37, Fig. 6B), further indicating that they represent two different zircon groups.

5.2. Whole-rock compositions

To better understand the source nature, genesis and mineralization mechanisms of the four trachytic lithofacies, we undertook whole-rock element and Nd isotopic analyses of these trachytic samples. Major and trace element compositions are presented in Table 2 and Nd isotopic data are listed in Table 3. Major element data for all the samples were recalculated on an anhydrous basis before being used for diagram plotting.

5.2.1. Major elements

All the samples have SiO_2 contents of 51.44 wt% to 60.24 wt%, and high alkaline ($Na_2O + K_2O$) contents of 10.04 wt% to 13.19 wt%. Based on the standard total-alkali-silica (TAS) classification diagram of Le Maitre et al. (1989), most Tudiling samples are plotted in the trachyte field, with the rest dispersed in adjacent fields, i.e., phonolite, tephriphonolite, and trachyandesite (Fig. 7A). In comparison, the MY and SXD syenites have relatively lower SiO_2 contents (50.09 wt% to 52.99 wt %) (Xu et al., 2008; Zhu et al., 2017), and are mostly plotted in the phonolite and tephriphonolite fields (Fig. 7A). The calculated peralkaline indices [PI = molar ($Na_2O + K_2O$)/Al_2O_3)] range from 1.29 to 1.66, indicating that these samples are exclusively peralkaline (PI > 1). They have Al_2O_3 and FeO^T contents varying from 20.97 wt% to 25.90 wt% and 0.90 wt% to 5.62 wt%, respectively. On the Al_2O_3 versus FeO^T classification scheme after MacDonald (1974), all the Tudiling trachytic samples fall in the comenditic trachyte field (Fig. 7B).

Regardless of the above similarities, the four lithofacies show some differences in their FeO^T, MnO, MgO, Na_2O, K_2O, and loss on ignition (LOI) contents. Among the three Silurian lithofacies, the phyllite samples have the highest Na_2O, MgO and LOI contents but the lowest K_2O contents (Table 2). The positive correlation between Na_2O and LOI but negative correlation between K_2O and LOI indicate that the hydrothermal alteration has led to the Na_2O gain but K_2O loss relative to the fresh samples (Fig. 8A and B), consistent with the petrographic observation of intensive albitization in these trachytic rocks (Fig. 3A–F). As for the Jurassic trachytic ignimbrite, they contain much higher FeO^T, MnO, Na_2O, P_2O_5 and LOI contents but lower K_2O contents than those of the Silurian trachytic rocks (Table 2). The correlations between Na_2O and K_2O contents and LOI contents for the trachytic ignimbrite (Fig. 8A and B) indicate the Na_2O loss and K_2O gain during hydrothermal alteration, consistent with the widespread sericitization in the ignimbrite (Fig. 3G and H).

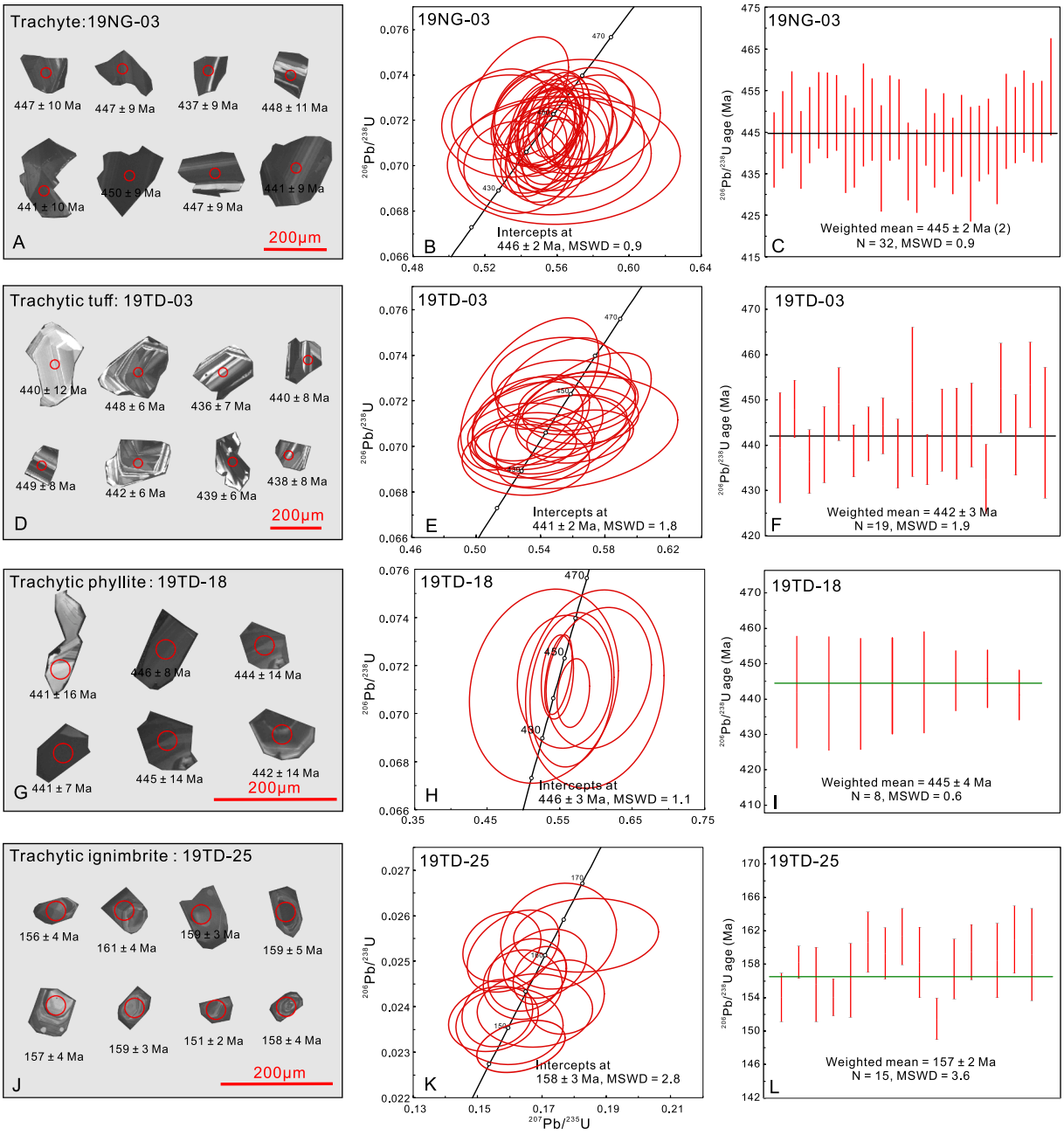

Fig. 5. Zircon CL images, laser spot locations and zircon U-Pb Wetherill plots and weighted mean $^{206}Pb/^{238}U$ age plots for the trachyte (A–C), trachytic tuff (D–F), trachytic phyllite (G–I), and trachytic ignimbrite (J–L) at Tudiling.

5.2.2. *Trace and REE elements*

Primitive mantle-normalized trace element and chondrite-normalized REE distribution patterns are given in Fig. 7C and D. All these trachyte samples are characterized by pronounced enrichments in Nb, Ta, Zr, and Hf but depletions in Sr, P, and Ti. Niobium contents in all these samples are higher than the lowest industrial grade (Nb_2O_5 contents: 0.08 wt%) and increase from the trachyte (543–618 ppm), trachytic ignimbrite (898–1260 ppm), trachytic tuff (939–1132 ppm) to trachytic phyllite (1570–1690 ppm) (Table 2 and Fig. 7E). Tantalum contents in the trachytic tuff and phyllite reach the lowest industrial grades (Ta_2O_5 contents: 0.01 wt%), varying from 76.55 ppm to 102.5 ppm and from 131.0 ppm to 138.8 ppm, respectively (Table 2 and Fig. 7E). The Nb/Ta ratios of most samples (except for the trachytic ignimbrite samples: 23–40) vary between 12 and 16.5, mostly within the typical ranges of continental crustal (12–13) and bulk silicate Earth (BSE) Nb/Ta ratios (14) (e.g., Münker et al., 2003) (Fig. 7E). Meanwhile, these samples display Zr enrichment with Zr concentrations from 316 ppm to 1670 ppm for the trachyte, and from 612 ppm to 1110 ppm for the trachytic tuff, and from 2410 ppm to 2610 ppm for the trachytic phyllite, and from 984 ppm to 1800 ppm for the trachytic ignimbrite, respectively (Table 2 and Fig. 7F). The Zr/Hf ratios of these samples cluster in two ranges, i.e., 38–59 (trachyte and trachytic ignimbrite samples) and 78–89 (trachytic tuff and trachytic phyllite samples), significantly higher than the chondritic value (34.4) (e.g., Münker et al., 2003) (Fig. 7F). The element pairs Zr/Hf and Nb/Ta ratios for most trachyte samples deviate from the chondritic values (34.4 and 19.9, respectively), which may be attributed to extreme fractionation or hydrothermal alteration (e.g., Huang et al., 2011; Niu, 2012).

As for their REEs, the trachytic ignimbrite samples possess the highest ΣREE contents (5221–6024 ppm), reaching the REE cut-off

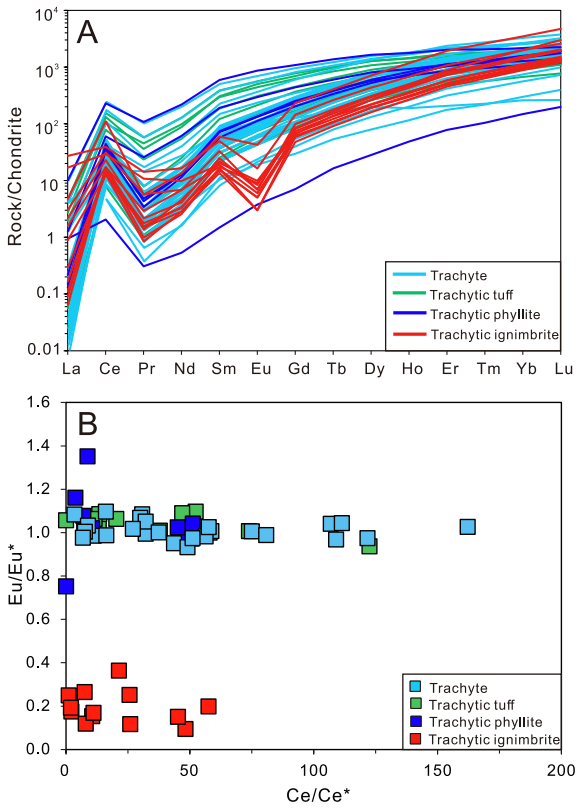

Fig. 6. (A) Zircon REE patterns and (B) Zircon Eu/Eu* vs. Ce/Ce* for the four trachytic lithofacies at Tudiling.

grade (REO contents: 0.5 wt%), while the other three types have significantly lower ΣREE contents ranging from 138 ppm to 703 ppm. Chondrite-normalized REE patterns indicate all the trachytic rocks are enriched in the light REEs (LREEs) relative to the heavy REEs (HREEs), with $(La/Yb)_N$ ratios from 13.01 to 62.82 for trachyte, 89.66 to 117.21 for trachytic ignimbrite, 64.14 to 86.24 for trachytic phyllite, and 261.66 to 318.45 for trachytic ignimbrite, respectively. All the trachyte samples display slightly to moderately negative Eu anomalies (δEu: 0.63–0.94) with the ignimbrite possessing the lowest δEu values (0.63–0.67), implying that plagioclase fractional crystallization happened to varying extent before the emplacement of these trachytic rocks.

Additionally, we applied the LOIs as the hydrothermal alteration indicator to plot against variations of fluid-mobile elements (Fig. 8C and D) and ore elements (Fig. 8E–H). Whole-rock Zr concentrations were used as the indicator for magma differentiation to decipher their co-variations with the other incompatible elements and ore metals (Fig. 9A–E). Their correlations would be carefully discussed in the section 6.2.

5.2.3. Samarium-Nd isotopic compositions

The εNd(t) values of the selected samples from the four trachytic lithofacies were calculated to their corresponding zircon weighted mean $^{206}Pb/^{238}U$ ages. Their εNd(t) values range from 2.3 to 3.4 for the trachyte, from 2.4 to 2.7 for the trachytic tuff, from 2.6 to 2.8 for the trachytic phyllite and from −2.9 to −2.8 for the trachytic ignimbrite, respectively (Table 3).

6. Discussion

6.1. Genesis of the Tudiling trachytic rocks

Previous studies on peralkaline magmatic rocks have led to general consensus that the peralkaline magmas can either be produced through protracted fractional crystallization of mafic/ultramafic magmas (e.g., Macdonald, 2012; Peccerillo et al., 2007), or represent partial melts of the crustal components, triggered by the thermal effect of upwelling mafic/ultramafic magmas (e.g., Avanzinelli et al., 2004; Trua et al., 1999). Meanwhile, both processes may be influenced by different degrees of crustal assimilation and/or magma mixing (e.g., Macdonald et al., 2015). The four trachytic lithofacies at Tudiling have evolved intermediate compositions (Table 2 and Fig. 7A), and thus their formation required magma ponding and differentiation at a shallow crust depth before eruption or emplacement at/near the surface. Zircon U–Pb dating indicates that the four trachytic lithofacies developed during two episodes of peralkaline magmatism, i.e., the early Silurian (445–442 Ma) and the late Jurassic (157 Ma). Phanerozoic tectonic reconstructions place the SQ to be an intraplate setting of the northern margin of the SCB during the early Silurian and be a post-collision orogen due to the closure of the Mianlue ocean during the late Jurassic (e.g., Dong et al., 2008; Meng and Zhang, 2000; Zhang et al., 2001; 2004). Both settings could have provided an extensional geodynamics for the generation of these peralkaline magmas. In the following parts, we discuss the petrogenesis of the two episodes of trachytic magmatisms separately.

The trachyte, trachytic tuff and trachytic phyllite developed during the early Silurian episode (445–442 Ma), and are coeval with their intrusive counterparts in the SQ, i.e., the MY syenite (442.6 ± 3.7 Ma, Zhu et al. (2017)) and SXD syenite (441.8 ± 2.2 Ma, Xu et al. (2008)). The three trachytic rocks share similar trace element (Nb, Ta, Zr, and Hf enrichments, but Sr, P, and Ti depletions), and REE (LREE enrichment and lacking ore-grades of ΣREE concentrations) patterns with the MY and SXD syenites (Fig. 7C and D). Moreover, the Silurian trachytic rocks display moderately depleted Nd isotope compositions (εNd(t) values: 2.3–3.4), which are within the range (εNd(t) values: 2.7–5.7, Zhu et al. (2017) and Xu et al. (2008)) of the MY and SXD syenites (Fig. 9F). The uniform and moderately depleted Nd isotopes in these Silurian peralkaline magmatic rocks preclude significant crustal assimilation and mixing of crust-derived magmas. Meanwhile, the evolved intermediate compositions of the Silurian trachytic rocks were most likely to represent the differentiated products of the mantle-derived magmas via protracted fractional crystallization. Actually, the Silurian mantle-derived rocks, like the Gaoping diabase (432 Ma, phlogopite $^{40}Ar/^{39}Ar$ plateau age, Huang et al. (1992)), the Zhengping diabase (451 ± 4 Ma, zircon U-Pb age, Xiang et al. (2016)) and the Langao lamprophyre (432 Ma, Xu et al. (2001)) have also been reported in the SQ. They are also characterized by moderately depleted εNd(t) values (1.8–4.0) as well as low $(^{87}Sr/^{86}Sr)_i$ compositions (0.70346–0.70365) (Huang et al., 1992; Xiang et al., 2016; Xu et al., 2001). Moreover, field observations indicate that some metagabbro/metadiabase have intruded into the strata of the southwestern Tudiling district and distributed near these trachytic rocks (Fig. 2). These Silurian mafic/ultramafic rocks in the SQ may represent the analogue of the mantle-derived magmas to generate the Silurian peralkaline rocks via protracted fractional crystallization. With regards to the mantle source nature of these Silurian peralkaline rocks, no consensus has been reached. Xu et al. (2008) and Zhu et al. (2017) suggested that their low initial Sr isotope compositions and high εNd(t) values approximate those of the HIMU components and some EMI components may have been involved due to the Pb isotope variations in their corresponding carbonatites. Chen et al. (2018) considered their mantle source represented the mixing product of two mantle components, i.e., the PREMA and a distinct radiogenic Pb reservoir. In this study, we would not make further deduction on the mantle source nature for the lack of other isotope information on the Tudiling trachytic samples, but it is expected that the Silurian trachytic rocks share a common mantle source with these coeval syenites and mafic/ultramafic rocks in the SQ (Fig. 10A).

Compared with the Silurian trachytic rocks, the Jurassic ignimbrite samples have higher FeO^T (2.94 wt%–5.62 wt%), MnO (0.51 wt%–1.53

Table 2
Whole-rock major, ore metal and trace element compositions of the Tudiling trachytic rocks.

Sample No.	19NG-01	19NG-02	19NG-04	19NG-05	19NG-06	19NG-07	19NG-08	19NG-09	19TD-01	19TD-02	19TD-03	19TD-04	19TD-05	19TD-06	19TD-07	19TD-08	19TD-18	19TD-19	19TD-20	19TD-21	19TD-22	19TD-23	19TD-25	19TD-26
Rock types	Trachyte								Trachytic								Trachytic phyllite				Trachytic ignimbrite			
Major elements (wt.%)																								
SiO_2	59.68	59.55	59.19	58.58	59.23	58.92	58.30	58.83	57.80	59.01	60.24	60.00	59.52	59.35	58.86	58.28	55.97	57.49	58.40	56.04	57.22	51.44	56.30	57.73
TiO_2	0.43	0.42	0.47	0.51	0.40	0.41	0.43	0.46	0.40	0.38	0.40	0.40	0.39	0.39	0.39	0.39	0.42	0.42	0.42	0.41	0.38	0.44	0.55	0.37
Al_2O_3	21.88	22.54	23.35	22.37	22.91	22.95	22.84	23.30	24.07	22.42	22.16	22.81	22.21	22.68	22.78	23.23	25.90	24.27	24.48	24.65	23.25	25.25	20.97	23.05
FeO^T	2.32	1.75	1.32	2.81	1.52	1.11	1.63	1.62	2.46	2.24	2.03	1.96	2.35	1.97	2.47	2.36	1.39	1.45	0.90	2.58	3.68	4.12	5.62	2.94
MnO	0.08	0.08	0.08	0.08	0.06	0.06	0.07	0.07	0.05	0.05	0.05	0.05	0.06	0.04	0.06	0.04	0.04	0.04	0.04	0.05	0.63	0.60	1.53	0.51
MgO	0.18	0.24	0.26	0.23	0.33	0.34	0.22	0.23	0.24	0.21	0.21	0.24	0.21	0.32	0.23	0.28	1.01	0.95	0.93	1.04	0.26	0.39	0.19	0.19
CaO	0.11	0.11	0.16	0.20	0.12	0.12	0.12	0.12	0.15	0.15	0.23	0.18	0.20	0.12	0.14	0.15	0.12	0.13	0.11	0.11	0.40	1.39	0.44	0.64
Na_2O	5.88	5.66	4.59	5.08	4.36	4.10	4.84	4.55	4.56	4.81	5.11	5.03	5.14	5.29	4.88	4.61	5.29	5.63	5.99	5.27	6.96	4.72	8.06	7.58
K_2O	6.77	7.06	7.98	7.71	8.83	8.96	8.26	8.29	7.81	7.88	7.39	6.65	7.41	7.47	7.81	8.22	5.47	5.26	5.14	5.66	3.91	6.00	1.99	3.14
P_2O_5	0.06	0.05	0.06	0.19	0.06	0.04	0.05	0.05	0.11	0.12	0.17	0.13	0.16	0.05	0.10	0.11	0.17	0.20	0.11	0.17	0.29	0.49	0.44	0.41
LOI	1.87	1.71	1.65	1.78	1.83	1.88	2.11	2.17	1.83	1.70	1.60	1.65	1.58	1.83	1.75	1.91	3.13	3.04	2.57	3.46	2.35	3.72	2.46	2.10
Total	99.94	99.86	99.74	100.14	100.21	99.48	99.51	100.30	100.06	99.56	100.18	99.73	99.84	100.15	100.06	100.16	99.70	99.67	99.94	100.16	100.15	99.35	99.43	99.59
Ore metals (wt.%)																								
ZrO_2	0.13	0.15	0.04	0.21	0.22	0.23	0.19	0.17	0.14	0.15	0.11	0.08	0.11	0.09	0.10	0.13	0.35	0.35	0.35	0.33	0.16	0.13	0.24	0.15
Nb_2O_5	0.08	0.08	0.08	0.09	0.09	0.08	0.09	0.09	0.16	0.14	0.15	0.21	0.16	0.13	0.17	0.15	0.24	0.24	0.23	0.22	0.13	0.13	0.18	0.13
Ta_2O_5	0.005	0.005	0.004	0.005	0.005	0.005	0.005	0.005	0.010	0.010	0.010	0.013	0.010	0.009	0.011	0.010	0.017	0.017	0.016	0.016	0.005	0.004	0.004	0.005
TREO	0.02	0.02	0.02	0.03	0.04	0.04	0.04	0.03	0.06	0.06	0.06	0.06	0.06	0.06	0.06	0.06	0.09	0.08	0.07	0.07	0.62	0.71	0.71	0.65
Trace elements (ppm)																								
Li	35.19	40.63	29.98	35.89	34.03	35.24	37.38	39.38	19.05	17.70	15.09	16.17	17.17	18.13	18.35	20.52	21.28	19.91	19.08	21.77	17.61	26.62	11.18	15.04
Be	7.67	8.56	11.07	9.32	13.11	13.73	14.55	15.09	18.60	17.37	16.10	15.73	16.50	17.55	17.89	21.19	31.30	29.23	28.58	30.54	15.02	23.56	8.37	13.38
P	243	210	266	900	260	180	214	191	536	541	745	626	752	206	435	495	788	925	506	778	1308	2201	2080	1965
Sc	3.81	4.18	1.99	5.61	6.01	6.00	5.11	4.81	3.76	3.87	3.09	2.55	3.12	2.59	2.90	3.45	8.62	8.59	8.74	8.05	5.22	5.82	6.65	5.08
Ti	2480	2411	2694	2960	2321	2426	2571	2709	2327	2181	2283	2312	2260	2261	2246	2268	2439	2409	2390	2336	2106	2442	3070	2057
V	32.0	36.7	48.6	44.3	42.1	43.4	42.3	43.4	32.0	29.4	25.7	29.1	28.4	31.3	31.2	38.1	31.6	31.3	31.4	34.2	70.4	206.2	36.6	123
Cr	0.36	0.39	0.90	0.61	0.40	1.74	0.34	0.48	0.13	1.20	0.21	0.13	0.14	0.25	0.64	0.26	0.11	0.21	0.15	0.85	0.50	0.51	0.57	0.56
Co	0.21	0.21	0.24	0.08	0.47	0.51	0.74	0.70	1.29	0.77	0.48	0.19	0.46	0.20	1.53	0.24	0.22	0.38	0.24	0.25	1.10	1.42	1.54	1.26
Ni	0.61	0.76	14.31	0.66	0.69	0.85	0.32	0.44	0.52	0.35	0.67	0.41	0.24	0.24	0.36	0.42	0.27	0.32	0.28	0.39	1.15	1.36	5.16	2.42
Cu	2.81	1.10	0.75	1.68	1.18	1.04	6.05	6.90	3.01	3.20	1.73	1.30	3.50	0.82	3.03	1.64	0.48	0.20	0.15	0.68	1.03	0.04	2.18	1.13
Zn	123.9	72.2	103.2	57.0	60.7	72.2	55.9	58.7	84.8	85.4	85.0	67.9	88.8	62.4	88.2	87.7	39.3	40.1	36.8	48.7	175	208	195	304
Ga	34.1	37.8	44.5	41.2	47.9	50.4	50.3	51.3	74.0	69.5	64.9	68.0	67.3	71.8	71.7	80.4	100.6	95.0	90.8	97.2	126	172	123	124
Rb	139	153	167	166	165	172	165	168	258	251	223	225	235	237	252	274	252	236	229	253	105	159	41.46	84.76
Sr	384	412	288	356	313	312	215	216	292	302	330	302	320	266	290	293	381	423	371	394	947	1376	752	1222
Zr	995	1133	316	1547	1634	1668	1381	1258	1032	1105	801	612	840	641	759	933	2609	2554	2610	2413	1191	984	1798	1133
Hf	12.12	13.72	4.24	19.68	21.0	20.9	17.2	15.9	20.8	20.5	20.7	13.1	14.5	16.9	12.9	20.8	58.9	59.2	60.7	52.9	13.6	12.4	20.3	12.7
Nb	552	543	543	618	608	572	614	602	1101	999	1063	1489	1116	939	1165	1021	1689	1681	1636	1569	910	898	1264	933
Mo	1.64	1.42	0.92	1.48	5.32	2.65	2.68	2.72	8.06	6.04	6.61	4.58	7.57	3.78	7.47	1.68	6.26	10.15	5.62	6.83	3.84	0.42	6.71	1.34
Sn	2.67	3.07	3.38	3.00	3.65	3.77	3.30	3.40	7.47	6.84	6.35	6.70	6.67	8.05	7.13	8.97	11.80	11.11	10.80	10.94	2.94	5.29	1.81	2.78
Sb	0.19	0.08	0.12	0.09	0.19	0.27	0.08	0.07	0.16	0.13	0.14	0.14	0.13	0.17	0.13	0.15	0.33	0.30	0.28	0.51	0.07	0.08	0.10	0.07
Cs	0.56	0.68	0.57	0.74	0.50	0.50	0.26	0.26	2.12	1.97	1.67	1.82	1.88	1.98	2.05	2.20	6.00	5.58	5.37	5.92	2.20	3.11	1.04	1.78
Ba	998	1049	1497	1295	2574	2738	2079	2149	2266	2222	2168	2060	2063	2272	2181	2262	3565	3368	3214	3480	4320	5950	2540	3501
La	35.6	46.8	53.6	64.8	75.8	90.3	83.8	76.9	152	150	136	145	147	151	142	151	208	189	152	181	1740	2018	2126	1847
Ce	62	85	92	103	128	154	138	127	241	239	221	233	233	247	225	243	328	301	250	284	2503	2836	2740	2617
Pr	6.36	8.71	9.45	10.10	12.48	15.08	13.49	12.40	22.94	22.83	21.31	22.55	22.27	24.19	21.89	23.75	30.77	28.97	24.72	27	215	248	254	226
Nd	20.79	27.85	30.59	32.82	40.17	49.61	44.22	40.68	74.00	73.58	68.43	72.49	71.79	78.42	69.07	76.76	98.77	96.19	87.87	86.72	614	700	724	644
Sm	3.46	4.14	4.54	4.97	6.06	7.29	6.77	6.34	9.95	9.98	9.21	9.68	9.88	9.49	9.17	10.24	12.65	13.06	13.31	11.60	56.61	64.21	65.70	59.25
Eu	1.02	1.17	1.10	1.44	1.68	2.00	1.90	1.77	2.25	2.34	2.20	2.23	2.32	2.12	2.09	2.39	2.97	3.18	3.25	2.76	12.03	13.76	14.08	12.57

(*continued on next page*)

Table 2 (*continued*)

Sample No.	19NG-01	19NG-02	19NG-04	19NG-05	19NG-06	19NG-07	19NG-08	19NG-09	19TD-01	19TD-02	19TD-03	19TD-04	19TD-05	19TD-06	19TD-07	19TD-08	19TD-18	19TD-19	19TD-20	19TD-21	19TD-22	19TD-23	19TD-25	19TD-26
Rock types	Trachyte								Trachytic								Trachytic phyllite				Trachytic ignimbrite			
Gd	3.16	3.77	4.14	4.53	5.52	6.63	5.87	5.48	8.09	8.24	7.69	8.02	8.28	7.18	7.49	8.24	10.76	10.74	9.87	9.57	53.50	70.87	61.28	56.06
Tb	0.46	0.51	0.44	0.60	0.74	0.85	0.75	0.70	0.76	0.83	0.75	0.77	0.83	0.63	0.71	0.78	1.09	1.09	1.05	1.00	3.84	4.55	4.42	3.98
Dy	2.46	2.68	1.92	3.07	3.82	4.29	3.62	3.39	2.99	3.44	2.89	3.00	3.30	2.42	2.80	3.04	4.64	4.65	4.55	4.44	12.44	13.45	14.22	12.74
Ho	0.45	0.50	0.31	0.57	0.71	0.79	0.65	0.61	0.50	0.58	0.47	0.47	0.52	0.42	0.46	0.49	0.80	0.79	0.78	0.77	2.06	2.11	2.34	2.09
Er	1.21	1.32	0.74	1.53	1.91	2.08	1.70	1.58	1.31	1.49	1.19	1.17	1.25	1.16	1.15	1.23	2.04	2.04	1.99	1.95	5.60	5.62	6.32	5.59
Tm	0.18	0.20	0.10	0.23	0.29	0.31	0.25	0.23	0.18	0.21	0.17	0.15	0.16	0.17	0.15	0.17	0.29	0.28	0.28	0.28	0.77	0.75	0.87	0.75
Yb	1.11	1.20	0.61	1.47	1.79	1.88	1.52	1.40	1.08	1.20	1.03	0.90	0.91	1.06	0.87	1.05	1.73	1.73	1.70	1.65	4.77	4.55	5.44	4.55
Lu	0.16	0.18	0.09	0.22	0.27	0.28	0.23	0.21	0.16	0.17	0.15	0.13	0.13	0.16	0.12	0.16	0.26	0.26	0.25	0.24	0.73	0.69	0.84	0.69
Y	12.46	13.51	8.52	15.48	20.08	22.82	16.58	15.39	12.12	13.97	11.31	10.76	12.08	11.10	10.97	12.43	21.66	21.80	21.61	21.34	54.93	53.89	61.70	54.56
Ta	38.54	37.19	32.85	42.83	40.27	39.98	43.56	43.58	80.73	80.02	81.58	102.52	84.72	76.55	88.37	79.35	138.84	136.02	132.48	130.98	39.57	28.80	31.34	37.42
Pb	5.38	46.37	15.92	13.97	12.91	18.97	21.32	21.44	8.11	10.52	10.64	7.73	9.40	6.17	9.34	9.93	23.37	17.53	11.67	13.15	23.57	25.41	55.62	28.72
Th	31.04	26.28	25.28	34.50	38.18	39.55	36.24	37.58	47.25	45.46	43.84	44.61	43.93	41.27	43.93	56.24	42.52	51.72	41.80	40.45	124	133	144	125
U	19.88	18.55	21.70	18.80	44.30	114.91	19.77	19.10	18.78	23.17	15.15	12.96	19.11	12.47	20.67	14.72	14.12	14.98	13.27	12.19	25.59	26.63	27.55	29.04
Zr/Hf	82	82	75	79	78	80	80	79	50	54	39	47	58	38	59	45	44	43	43	46	88	79	89	89
Nb/Ta	14	15	17	14	15	14	14	14	14	12	13	14	13	12	13	13	12	12	12	12	23	31	40	25
ΣREE	151	197	208	245	299	358	319	294	529	528	484	510	514	537	494	535	725	675	573	634	5276	6042	6085	5553
$(La/Yb)_N$	23	28	63	32	30	34	40	39	101	90	95	116	116	102	117	103	86	78	64	79	262	318	281	292
δEu	0.94	0.91	0.78	0.93	0.89	0.88	0.92	0.92	0.77	0.79	0.8	0.77	0.78	0.79	0.77	0.8	0.78	0.82	0.87	0.8	0.67	0.63	0.68	0.67

wt%), P_2O_5 (0.29 wt%–0.49 wt%), Th (124–144 ppm) and ΣREEs (5276–6085 ppm) contents, consistent with their higher volumes of Fe-Mn-oxides (Fig. 3G and H) and monazite in their mineral compositions (Fig. 4F and G). The trachytic ignimbrite samples exhibit enriched Nd isotope compositions (εNd(t) values: −2.9–−2.8, Table 3 and Fig. 9F), implying two possible origins, i.e., continental crust-derived or enriched mantle-derived. The Jurassic trachytic ignimbrite samples do not follow the magma differentiation trend constructed by the Silurian trachytic samples (Fig. 9A–C), precluding a continued evolution from the Silurian trachytic samples. Moreover, the partial melting and contamination of the crustal components unlikely occurred because most continental crust-derived components are generally poor in Fe, Mn, and P, and no Fe-Mn-P deposits have ever been explored near the Tudiling district. During the late Jurassic, the trachytic ignimbrite developed in a post-collision extensional setting due to the subduction and closure of the Mianlue ocean slab during the Permian to the middle Triassic (Dong et al., 2011; Dong and Santosh, 2016). As a result, the mantle source of the Jurassic trachytic ignimbrite may have been modified by the residuals of the Mianlue ocean sediments (Fig. 10D). Meanwhile, the oceanic sediments were likely rich in Fe-Mn and LREE contents (e.g., Fe-Mn nodules) and have significantly negative δEu anomalies (e.g., Elderfield et al., 1981; Nagasawa et al., 1979), and hence their addition to the mantle source may provide a reasonable interpretation for the unique features and enriched mantle source of the Jurassic ignimbrite.

6.2. *Mechanism of the Tudiling Nb-Ta-Zr-REE enrichment*

Three Silurian trachytic rocks are characterized by Nb-Ta-Zr enrichment/mineralization with the phyllite possessing the highest grades of rare metal concentrations, whereas the Jurassic ignimbrite displays Nb-Ta-Zr-REE enrichment/mineralization (Table 2). This is consistent with the petrographic observation that the phyllite contains more Nb-Ta-Zr-rich mineral phases and the ignimbrite has more REE-rich mineral phases than the rest lithofacies (Fig. 4). Among these ore minerals, columbite of medium sizes (50–100 μm) represents the major primary Nb(-Ta)-rich mineral (Ta content: ~5.80 wt%, see EDS results in Supplementary Materials), and displays evident metasomatism relationship with ilmenite and ilmenorutile (Fig. 4C and D). In the phyllite, some tiny and anhedral ilmenorutile grains disperse along the microfolds and microfractures, implying significant Nb re-mobilization and precipitation. Zircon and apatite of large grains represent the major primary Zr and REE-rich minerals, respectively, and most of them have been subjected to hydrothermal metasomatism to some extents (Fig. 4A and F). Monazite grains are mostly anhedral, small in size, and stardust-like in distribution, and represent the REE-rich secondary minerals. They display close spatial relationship with the albitization and sericitization, indicating they were the reprecipitation products of REE-rich fluids. Other secondary REE minerals (bastnaesite and allanite) occur as the metasomatic phase of early-crystalized minerals, like augite (Fig. 4H), or display intergrowth relationship with albite (Fig. 4I), further implying that hydrothermal metasomatism may have caused rare metal mobilization and reprecipitation at Tudiling.

The broad positive correlations between incompatible elements (Y, Ce, Th, Nb, and Ti) and Zr (Fig. 9A–E) for both the Silurian and Jurassic trachytic samples favors the initial Zr-Nb-REE enrichment through protracted magmatic differentiation. The high REE and Th concentrations in the Jurassic trachytic samples may have been inherited from an enriched mantle source modified by the residues of the Mianlue ocean sediments. Moreover, no evidence for liquid immiscibility exists, as has been suggested as a critical magmatic differentiation process for upgrading rare metal concentrations in the Toongi peralkaline systems (Spandler and Morris, 2016). Petrographic observation indicates that most of the Tudiling trachytic rocks have been subjected to varying degrees of hydrothermal alteration, which had likely affected the chemical compositions of these rocks to some extent. As for the Silurian trachytic rocks, the phyllite is more intensively altered than the trachyte

Table 3
Whole-rock Nd isotope compositions of the Tudiling trachytic rocks.

Sample	Sm (ppm)	Nd (ppm)	$^{147}Sm/^{144}Nd$	$^{143}Nd/^{144}Nd$	2σ	$(^{143}Nd/^{144}Nd)_i$	εNd(t)	$T_{DM,1}$ (Ma)
Trachyte								
19NG-01	3.46	20.79	0.10596	0.512491	0.000008	0.51218	2.3	933
19NG-02	4.14	27.85	0.09200	0.512505	0.000009	0.51224	3.4	808
19NG-05	4.97	32.82	0.09371	0.512499	0.000009	0.51223	3.1	828
Trachytic tuff								
19TD-01	9.95	74.00	0.08128	0.512431	0.000004	0.51220	2.5	828
19TD-03	9.21	68.40	0.08140	0.512427	0.000005	0.51219	2.4	833
19TD-06	9.49	78.40	0.07318	0.512419	0.000004	0.51221	2.7	794
Trachytic phyllite								
19TD-18	12.65	98.77	0.07771	0.512435	0.000005	0.51221	2.8	801
19TD-19	13.06	96.19	0.08232	0.512435	0.000004	0.51220	2.6	829
19TD-20	13.31	87.87	0.09147	0.512471	0.000005	0.51220	2.7	847
Trachytic ignimbrite								
19TD-22	56.61	614	0.05573	0.512346	0.000005	0.51229	-2.9	776
19TD-23	64.21	700	0.05544	0.512352	0.000004	0.51229	-2.8	769
19TD-25	65.70	724	0.05486	0.512351	0.000005	0.51229	-2.8	768

Note: $(^{147}Sm/^{144}Nd)_{CHUR} = 0.1967$ (Jacobsen and Wasserburg, 1980) and $(^{143}Nd/^{144}Nd)_{CHUR} = 0.512638$ (Goldstein et al., 1984) were used for the calculations. $\lambda_{Sm} = 6.54 * 10^{-12}$ year^{-1}.

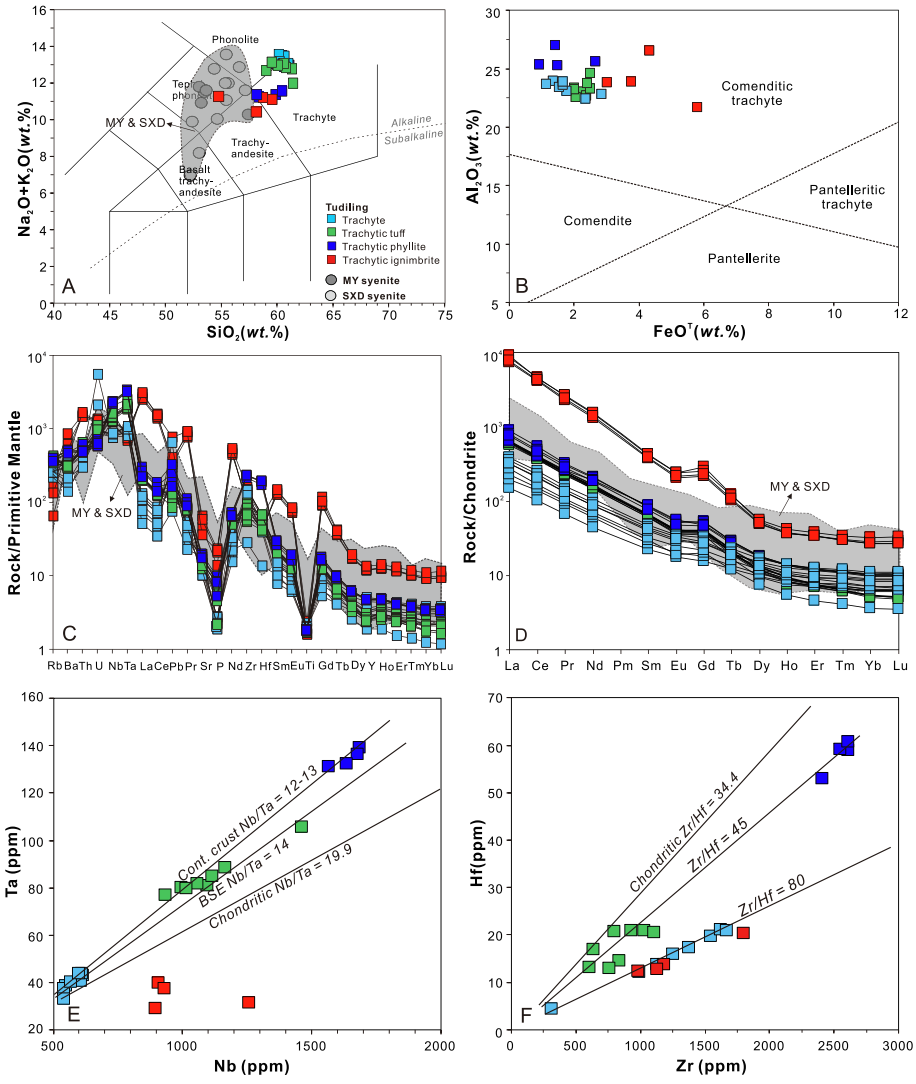

Fig. 7. The geochemical classification diagram for Tudiling trachytic rocks. (A) Chemical compositions of the four trachytic lithologies plotted on the total alkali–silica (TAS) diagram of Le Bas et al. (1986). (B) Peralkaline compositions for the Tudiling trachytic rocks plotted on the Al_2O_3 vs. FeO^T classification scheme for oversaturated peralkaline rocks (MacDonald, 1974). (C) Trace element and (D) REE distribution patterns of the Tudiling trachytic rocks. The major and trace elements of the MY syenite (Zhu et al., 2017) and the SXD syenite (Xu et al., 2008) (grey shaded areas) were applied for comparison. The primitive mantle and chondrite values for normalization refer to Sun and McDonough (1989). (G) Ta vs. Nb and (H) Hf vs. Zr concentration plots for the Tudiling trachytic rocks.

and trachytic tuff, as was reflected in the higher LOI contents (Table 2 and Fig. 8) and more secondary minerals in the phyllite (Fig. 3G–H and Fig. 4E). On the alteration indicator plots (Fig. 8A–D), for the Silurian trachytic rocks, their Na_2O, Rb and Ba contents increase but K_2O contents decrease from the intensively altered phyllite to the less altered trachytic rocks, supported by the petrographic observation of the

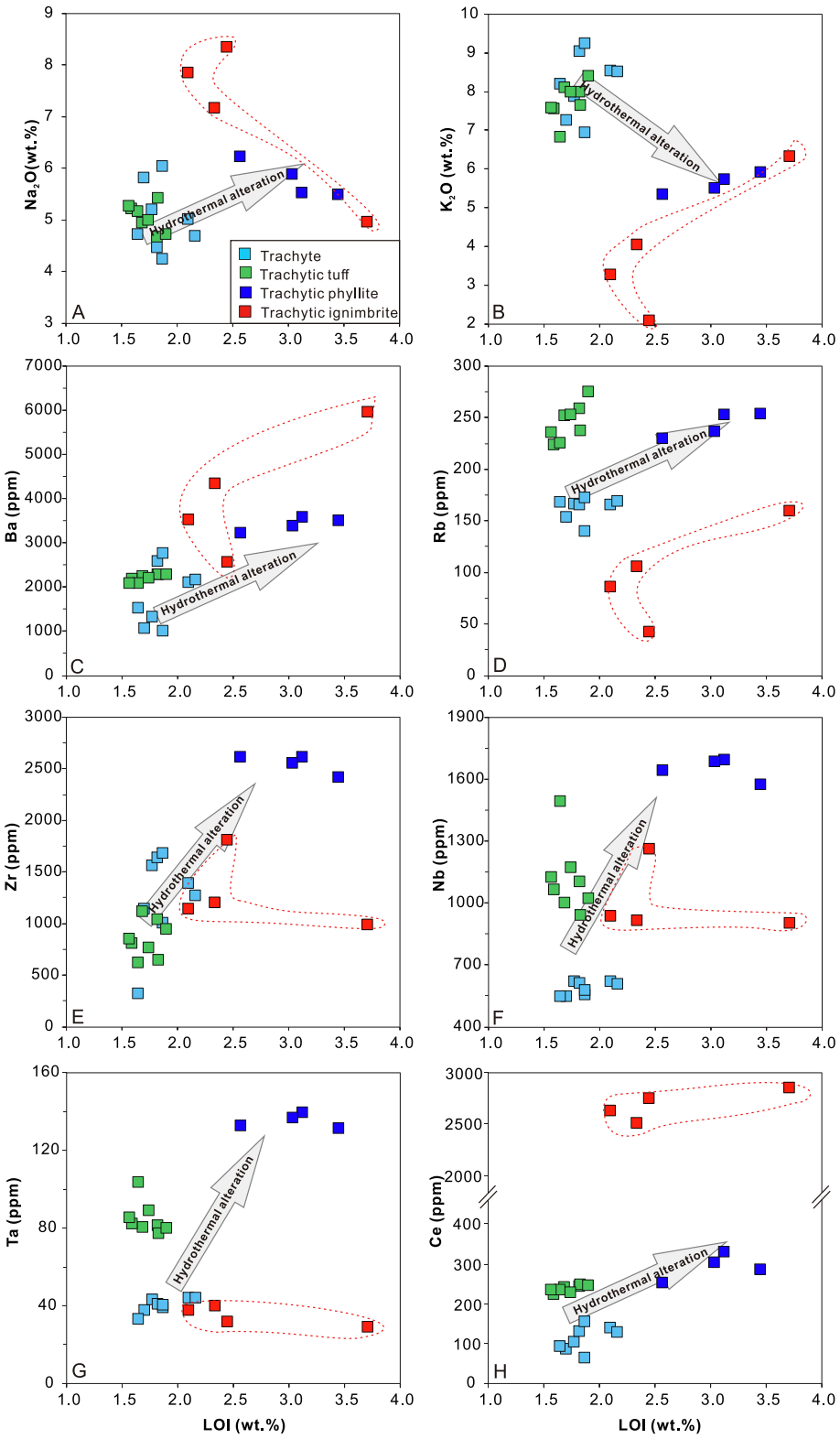

Fig. 8. Scatterplots of the geochemical indicators of hydrothermal alteration for the Tudiling trachytic rocks. (A) Na_2O vs. loss-on-ignition (LOI), (B) K_2O vs. LOI, (C) Ba vs. LOI, (D) Rb vs. LOI, (E) Zr vs. LOI, (F) Nb vs. LOI, (G) Ta vs. LOI and (H) Ce vs. LOI.

widespread albitization in the Tudiling trachytic rocks (Fig. 3). Meanwhile, such hydrothermal alteration may have upgraded Zr-Nb-Ta-REE enrichment as indicated by the broad positive correlation between the Zr-Nb-Ta-Ce contents and LOI for the Silurian samples (Fig. 8E–H), providing a reasonable interpretation for the higher grades of Nb-Ta-Zr-REE concentrations in the phyllite. As for the Jurassic trachytic ignimbrite, their K_2O, Rb, and Ba contents are positively but Na_2O contents are negatively correlated with their LOI contents (Fig. 8A–D), indicating that hydrothermal alteration caused Na loss but K gain in the altered rocks, similar to the alteration mechanism of the Toongi high Th-U trachytic samples reported by Spandler and Morris (2016). In contrast, the ignimbrite samples have nearly consistent Zr, Nb, Ta and Ce contents

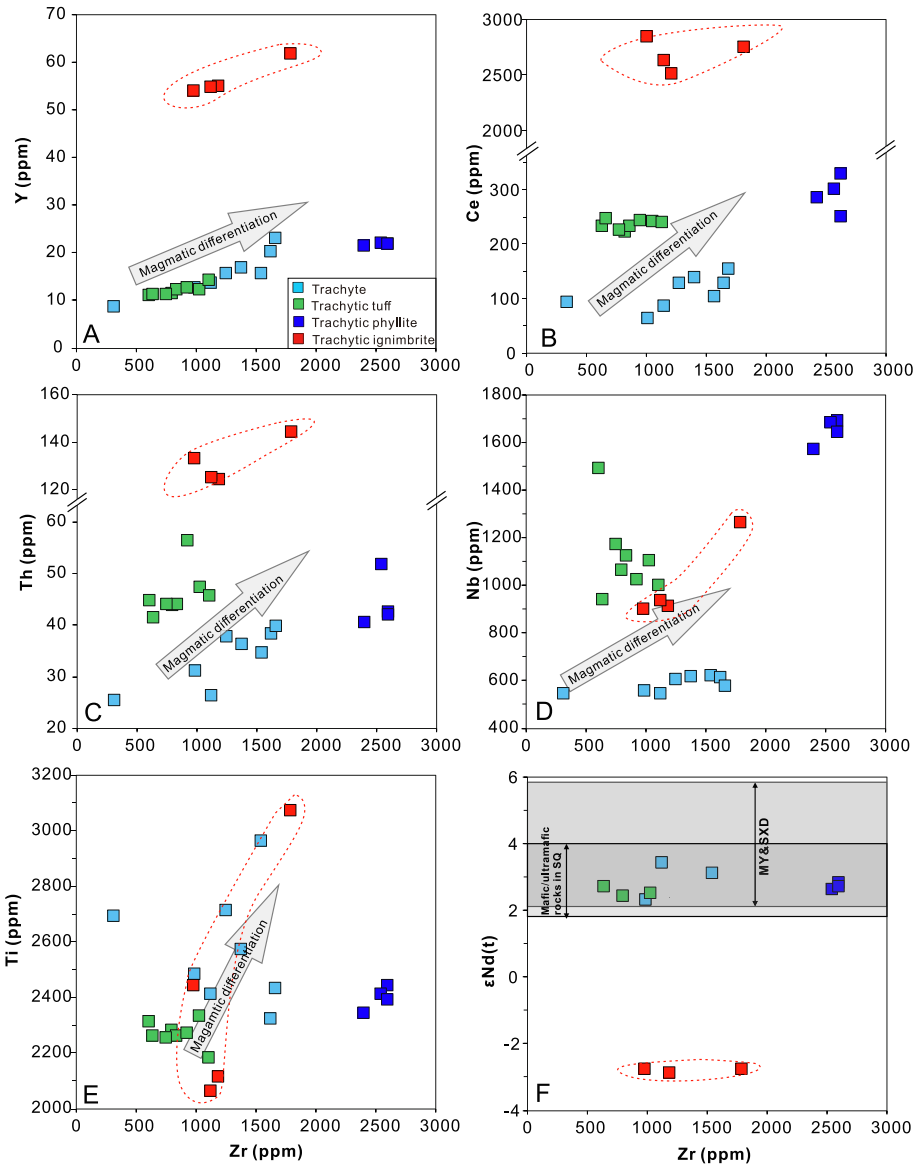

Fig. 9. Scatterplots of ore and other incompatible elements for the Tudiling trachytic rocks. (A) Y vs. Zr, (B) Ce vs. Zr, (C) Th vs. Zr, (D) Nb vs. Zr, (E) Ti vs. Zr and (F) εNd(t) vs. Zr. In Fig. 9F, the grey shaded regions represent the εNd(t) ranges of the MY and SXD syenites and the Silurian mafic rocks.

regardless of the LOIs variations (Fig. 8D and E), implying that the alteration did not upgrade the Zr-Nb-REE concentrations in the ignimbrite. This observation is also consistent with Spandler and Morris (2016)'s conclusions that such hydrothermal alteration had only caused relatively limited and localized rare metal mobilization in the trachytic ignimbrite.

6.3. *Implications for rare metal mineralization of extrusive peralkaline systems*

Together with previous investigations on the peralkaline magmatic systems, our results confirmed that melting of an enriched mantle source and protracted fractional crystallization of alkaline magmas play a leading role in the initial enrichment of rare metals. Hydrothermal alteration could cause rare metal mobilization from primary Nb-REE minerals, but may have distinct effects on the different lithofacies. For instance, based on the study of the Brockman volcanic-hosted rare-metal deposit, Ramsden et al. (1993) proposed that the alteration and remobilization of magmatic precursor minerals (mainly columbite and zircon) by F-rich deuteric solutions had played a dominant role in causing the rare metal mineralization in the Niobium tuff. In contrast, Spandler and Morris (2016) emphasized that the Ca-rich hydrothermal fluids had only triggered limited and localized remobilization of rare metals and had not upgraded rare metal concentrations in the Toongi deposit. In the Tudiling case, the hydrothermal alteration was expected to have triggered Zr, Nb, Ta, and REE remobilization in primary ore mineral phases (Fig. 4 and Fig. 10B) by SO_4^{2-}-rich and fluorine-rich hydrothermal fluids (the occurrences of Fe sulfates, sericite, bastnaesite and allanite in phyllite, Fig. 3F and Fig. 4) and led to the reprecipitation of tiny secondary Nb-REE minerals (Fig. 4 and Fig. 10B and C). Nevertheless, the effects of hydrothermal alteration on rare metal upgrading are highly dependent on the rock structures and distinct on the intensively altered phyllite and ignimbrite. The trachytic phyllite was structurally intensively altered during phyllitization and developed plenty of microfolds and microfractures, providing sufficient space for the precipitation of the secondary ore minerals (Fig. 10C). In contrast, the Jurassic trachytic ignimbrite is structurally pyknotic (Fig. 3G and H), and lacks in sufficient space for the mobilization and precipitation of ore-bearing fluids. Hence, the hydrothermal alteration had only led to very localized mobilization of rare metals and no extra rare metal inputs

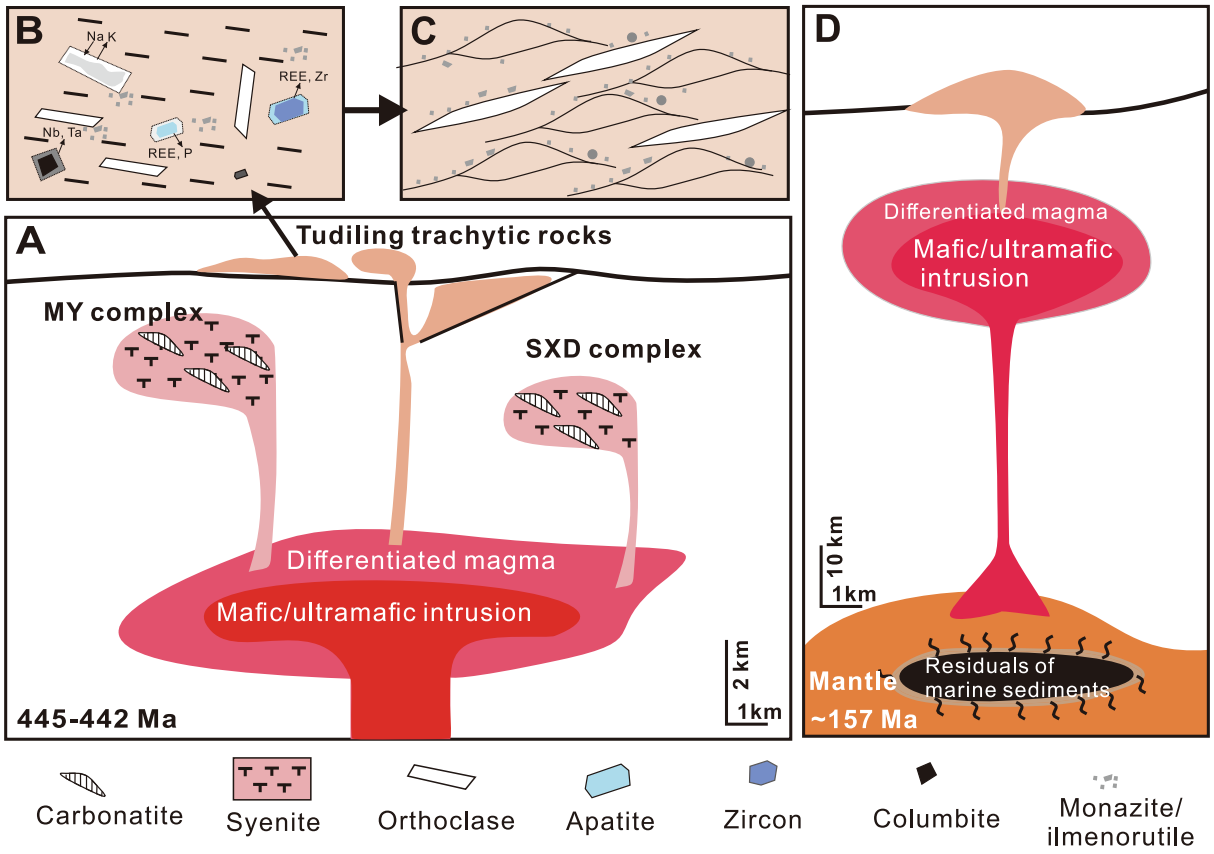

Fig. 10. Schematic diagram showing the generation of the peralkaline magmas and related rare metal enrichment/mineralization. (A) Evolution of the Silurian trachytic rocks at Tudiling and syenites at MY and SXD. (B) Cartoon showing the alteration of the precursor magmatic minerals (i.e., orthoclase, zircon, apatite and columbite) and the reprecipitation of tiny secondary ore minerals (i.e., monazite and ilmenorutile). (C) Abundant precipitation of secondary ore minerals along the microfolds and microstructures during the phyllitization. (D) The evolution of the Jurassic trachytic ignimbrite at Tudiling.

Table 4
Comparisons between the Tudiling trachyte deposit and the MY and SXD syenite deposits in the SQ and other extrusive peralkaline rock rare metal deposits investigated worldwide.

Deposit	Location/Country	Peralkaline rock types	Grades (*wt.*%)	Ore tonnages	References
Tudiling	South Qinling, China	Trachyte	0.17% ZrO_2, 0.08% Nb_2O_5, 0.005% Ta_2O_5, & 0.03% TREO	122.5 Mt (105 Kt Nb_2O_5, 2.7 Kt Ta_2O_5)	Xiong et al. (2018)
		Trachytic tuff	0.10% ZrO_2, 0.16% Nb_2O_5, 0.01% Ta_2O_5, & 0.06% TREO		
		Trachytic phyllite	0.34% ZrO_2, 0.24% Nb_2O_5, 0.02% Ta_2O_5, & 0.08% TREO		
		Trachytic ignimbrite	0.17% ZrO_2, 0.14% Nb_2O_5, 0.004% Ta_2O_5, & 0.67% TREO		
Miaoya		Syenite(-carbonatite)	0.09% ZrO_2, 0.12% Nb_2O_5, 0.003% Ta_2O_5, & 0.14% TREO	——	Zhu et al. (2017)
Shaxiongdong		Syenite(-carbonatite)	0.08% ZrO_2, 0.05% Nb_2O_5, 0.001% Ta_2O_5, & 0.07% TREO	——	Xu et al. (2008)
Brockmans	Western Australia	Trachytic tuff	0.79% ZrO_2, 0.3% Nb_2O_5, 0.1% Y_2O_3, & 0.023% Ta_2O_5	22 Mt	Ramsden et al. (1993)
Toongi	New South Wales, Australia	Trachyte	1.93% ZrO_2, 0.89% TREO, O.46% Nb_2O_5, 0.03% Ta_2O_5, & 0.04% HfO_2	73.2 Mt	Spandler and Morris (2016)
Peak Range	Queensland, Australia	Augite/hornblende trachyte, Arfvedsonite/ hornblende/Aegirine rhyolite	0.55% ZrO_2, 0.13% TREO, 0.09% Nb_2O_5, 0.012% HfO_2, & 0.005% Ta_2O_5	593 Mt	Chandler and Spandler (2020)
Foxtrot	Labrador, Canada	Pantellerite/comendite	1.3% ZrO_2, 1.07% TREO, & 0.08% Nb_2O_5	3.4 Mt	Miller (2015)
Round Top Mountain	Texas, America	Rhyolite	0.06% TREO	231 Mt	Pingitore et al. (2014)

Note: The rare metal mineralization of the Miaoya and Shaxiongdong deposits are related to both syenite and carbonatite, but only the syenite related rare metal grades are employed for comparison.
TREO is short for Total rare earth oxides. Kt: kiloton; Mt: million tons.

occurred in the ignimbrite.

The Tudiling trachytic rocks have Nb-Ta concentrations reaching the lowest industrial grades and Zr concentrations close to Zr cut-off grade, which are much higher than those of the MY and SXD syenites near the Tudiling (Table 4). Such differences may be attributed to the higher degree of magmatic differentiation of the Silurian Tudiling trachytic rocks than that of the MY and SXD syenites, as indicated by their higher whole-rock Zr contents in the Tudiling trachytic rocks. Alternatively, the MY and SXD syenites might simply represent the products of mantle partial melting without any differentiation. Additionally, distinguished from the other peralkaline rock associated rare metal deposits in the SQ, the Tudiling deposit has obvious Ta mineralization (predominantly hosted in columbite with Ta contents of ~ 5.8 wt%) in the trachytic tuff and phyllite (Table 4). This may be partly due to the higher solubility of Ta relative to Nb in high-fluorine hydrothermal fluids (Keppler, 1993; Xiong et al., 1998), leading to economically viable Ta enrichment after the precipitation of Ta-bearing complexes under low temperature conditions. Estimated from the surface exposure area and the true thickness of the eight orebodies, the Tudiling deposit contains a total ore reserve of 122.7 million tons (105 kilotons Nb_2O_5 and 2.7 Kilotons Ta_2O_5) (Xiong et al., 2018), making the Tudiling deposit a potential large-scale Nb-Ta deposit. However, when compared with typical trachyte rare metal deposits, such as the Brockman and Toongi deposits in Australia, the Tudiling deposit exhibit significantly lower grades of rare metals but much higher tonnages of ore reserves (Table 4). The REE mineralization of the Tudiling is mainly related to the Jurassic trachytic ignimbrite, which has similar REE grades to the Brockman and Toongi trachytes (Table 4). However, the distribution of the Jurassic trachyte ignimbrite is currently not well constrained, and its TREO reserves of the Tudiling need further investigations. The Tudiling deposit is only a representative of the trachyte associated Nb(-Ta-Zr-REE) deposits in the SQ, and the other cases, such as the Tianbao, Heihuzhai, Zhujiayuan, Shuanghekou and Haoping deposits had also been explored and cluster in the Northern Daba Mountains and Wudang Uplift of the SQ. In the near future, with the increasing demand for rare metals and the advance of rare metal extraction techniques, we believe that these rare metal resources in the SQ could become an important supply for rare metal exploitation.

7. Conclusions

(1) The four trachytic lithofacies at Tudiling formed during two episodes, i.e., 445–442 Ma (early Silurian) and 157 Ma (late Jurassic). The Silurian trachytic rocks (i.e., trachyte, trachytic tuff and trachytic phyllite) are coeval and geochemically similar with their intrusive counterparts, i.e., the MY and SXD syenites. These Silurian alkaline rocks developed due to protracted fractional crystallization of mantle-derived magmas. The Jurassic trachytic ignimbrite is geochemically distinct and has higher FeO, MnO, Th and REE contents and enriched Nd isotope compositions. It may have been generated by partial melting of an enriched mantle source, modified by residuals of the Mianlue oceanic sediments.

(2) Rare metal enrichment in these trachytic rocks were initially attributed to the melting of an enriched mantle and subsequent protracted crystallization fractionation of alkaline mafic magmas. Effects of hydrothermal alteration on rare metal upgrading are highly dependent on the rock structures and distinct on the intensively altered trachytic phyllite and ignimbrite. The phyllite had developed plenty of microfolds and microfractures during phyllitization, providing sufficient space for the input and precipitation of mobilized rare metals.

Declaration of Competing Interest

The authors declare that they have no known competing financial interests or personal relationships that could have appeared to influence the work reported in this paper.

Acknowledgements

This work was funded by the National Natural Science Foundation of China (41930424 and 41903016), the National Key R&D Program of China (2017YFC0602301), the Science and Technology Planning Project of Guangdong Province, China (2020B1212060055), and the GIGCAS President Youth Foundation of 2019SZJJ-08. We thank editor Huayong Chen and guest editor Yan Liu for their efficient handling of this paper. The final version of the manuscript benefits from the constructive comments from Dr. Mingqian Wu and the other two anonymous reviewers. This is contribution No.IS-3085 from GIGCAS.

Appendix A. Supplementary data

Supplementary data to this article can be found online at https://doi.org/10.1016/j.oregeorev.2021.104535.

References

Avanzinelli, R., Bindi, L., Menchetti, S., Conticelli, S., 2004. Crystallisation and genesis of peralkaline magmas from Pantelleria Volcano, Italy: an integrated petrological and crystal-chemical study. Lithos 73, 41–69.
Chakhmouradian, A.R., Wall, F., 2012. Rare earth elements: minerals, mines, magnets (and more). Elements 8, 333–340.
Chakhmouradian, A.R., Zaitsev, A.N., 2012. Rare earth mineralization in igneous rocks: sources and processes. Elements 8, 347–353.
Chandler, R., Spandler, C., 2020. The igneous petrogenesis and rare metal potential of the peralkaline volcanic complex of the southern Peak Range, Central Queensland, Australia. Lithos 358–359, 105386.
Chen, W., Lu, J., Jiang, S.-Y., Ying, Y.-C., Liu, Y.-S., 2018. Radiogenic Pb reservoir contributes to the rare earth element (REE) enrichment in South Qinling carbonatites. Chem. Geol. 494, 80–95.
Çimen, O., Kuebler, C., Monaco, B., Simonetti, S.S., Corcoran, L., Chen, W., Simonetti, A., 2018. Boron, carbon, oxygen and radiogenic isotope investigation of carbonatite from the Miaoya complex, central China: evidences for late-stage REE hydrothermal event and mantle source heterogeneity. Lithos 322, 225–237.
Dong, Y., Zhang, G., Neubauer, F., Liu, X., Genser, J., Hauzenberger, C., 2011. Tectonic evolution of the Qinling orogen, China: review and synthesis. J. Asian Earth Sci. 41, 213–237.
Dong, Y.P., Santosh, M., 2016. Tectonic architecture and multiple orogeny of the Qinling Orogenic Belt, Central China. Gondwana Res. 29, 1–40.
Dong, Y.P., Zha, X.F., Fu, M.Q., Zhang, Q., Zhang, Y., 2008. The structures of the Dabashan fold-thrust belt, southern Qinling, China. Geol. Bull. China 27, 1493–1508.
Dostal, J., Kontak, D.J., Karl, S.M., 2014. The Early Jurassic Bokan Mountain peralkaline granitic complex (southeastern Alaska): Geochemistry, petrogenesis and rare-metal mineralization. Lithos 206, 456–456.
Elderfield, H., Hawkesworth, C.J., Greaves, M.J., Calvert, S.E., 1981. RARE-EARTH ELEMENT GEOCHEMISTRY OF OCEANIC FERROMANGANESE NODULES AND ASSOCIATED SEDIMENTS. Geochim. Cosmochim. Ac 45, 513–528.
Goldstein, S.L., Onions, R.K., Hamilton, P.J., 1984. A Sm–Nd isotopic study of atmospheric dusts and particulates from major river systems. Earth Planet. Sci. Lett. 70, 221–236.
Huang, H., Niu, Y., Zhao, Z., Hei, H., Zhu, D., 2011. On the enigma of Nb-Ta and Zr-Hf fractionation—A critical review. J. Earth Sci. 22, 52–66.
Huang, Y., Ren, Y., Xia, L., Xia, Z., Zhang, C., 1992. The early Paleozoic bimodal volcanism of the Northern Dabashan: case study on the Gaotan diabase and Gaoping trachyte. Acta Petrol. Sin. 31, 243–256.
Jacobsen, S.B., Wasserburg, G.J., 1980. Sm–Nd isotopic evolution of chondrites. Earth Planet. Sci. Lett. 50, 139–155.
Keppler, H., 1993. Influence of fluorine on the enrichment of high field strength trace elements in granitic rocks. Contributions Mineral. Petrol. 114, 479–488.
Le Bas, M., Le Maitre, R., Streckeisen, A., Zanettin, B., 1986. A chemical classification of volcanic rocks based on the total alkali-silica diagram. J. Petrol. 27, 745–750.
Le Maitre, R.W.B., Dudek, P., Keller, A., Lameyre, J., Le Bas, J., Sabine, M., Schmid, P., Sorensen, R., Streckeisen, H., Woolley, A., 1989. A classification of igneous rocks and glossary of terms: Recommendations of the International Union of Geological Sciences, Subcommission on the Systematics of Igneous Rocks. International Union of Geological Sciences.
Li, M.Y.H., Zhou, M.F., Williams-Jones, A.E., 2020. Controls on the dynamics of rare earth elements during subtropical hillslope processes and formation of regolith-hosted deposits. Econ. Geol. 115, 1097–1118.
Li, S., 1980. Geochemical features and petrogenesis of Miaoya carbonatites, Bubei. Geochimica 4, 345–355.
Liang, X.R., Wei, G.J., Li, X.H., Liu, Y., 2003. Precise measurement of 143Nd/144Nd and Sm/Nd ratios using multiple-collectors inductively coupled plasma-mass spectrometer (MC-ICPMS). Geochimica 32, 91–96.
Ling, W.L., Ren, B.F., Duan, R.C., Liu, X.M., Mao, X.W., Peng, L.H., Liu, Z.X., Cheng, J.P., Yang, H.M., 2008. Timing of the Wudangshan, Yaolinghe volcanic sequences and mafic sills in South Qinling: U-Pb zircon geochronology and tectonic implication. Chinese Sci. Bull. 53, 2192–2199.

Ludwig, K.R., 2012. Isoplot 3.75: A Geochronological Toolkit for Microsoft Excel. Berkeley CA: Berkeley Geochronology Center Special Publication 5, 1-75.
MacDonald, R., 1974. Nomenclature and petrochemistry of the peralkaline oversaturated extrusive rocks. Bull. Volcanologique 38, 498–516.
Macdonald, R., 2012. Evolution of peralkaline silicic complexes: lessons from the extrusive rocks. Lithos 152, 11–22.
Macdonald, R., Sumita, M., Schmincke, H.-U., Bagiński, B., White, J.C., Ilnicki, S.S., 2015. Peralkaline felsic magmatism at the Nemrut volcano, Turkey: impact of volcanism on the evolution of Lake Van (Anatolia) IV. Contribut. Mineral. Petrol. 169, 34.
Meng, Q.-R., Zhang, G.-W., 2000. Geologic framework and tectonic evolution of the Qinling orogen, central China. Tectonophysics 323, 183–196.
Miller, R.R., 2015. Pantellerite-hosted rare earth element mineralisation in southeast Labrador: The Foxtrot deposit. Symposium on Strategic and Critical Materials Proceedings, November 13–14, 2015, Victoria, British Columbia.
Münker, C., Pfander, J.A., Weyer, S., Buchl, A., Kleine, T., Mezger, K., 2003. Evolution of planetary cores and the earth-moon system from Nb/Ta systematics. Science 301, 84–87.
Nagasawa, H., Yamakoshi, K., Shimamura, T., 1979. Trace element concentrations in silicate spherules from oceanic sediments. Geochim. Cosmochim. Ac 43 (267–269), 271–272.
Nie, X., Wang, Z., Chen, L., Yin, J., Xu, H., Fan, L., Chen, P., Wang, G., 2020. Mineralogical constraints on Nb–REE mineralization of the Zhujiayuan Nb (−REE) deposit in the North Daba Mountain, South Qinling, China. Geol. J. 55, 4845–4863.
Niu, Y., 2012. Earth processes cause Zr–Hf and Nb–Ta fractionations, but why and how? RSC Adv. 2, 3587–3591.
Paton, C., Hellstrom, J., Paul, B., Woodhead, J., Hergt, J., 2011. Iolite: Freeware for the visualisation and processing of mass spectrometric data. J. Anal. Atom. Spectrom. 26, 2508–2518.
Pearce, N.J.G., Perkins, W.T., Westgate, J.A., Gorton, M.P., Jackson, S.E., Neal, C.R., Chenery, S.P., 1997. A compilation of new and published major and trace element data for NIST SRM 610 and NIST SRM 612 glass reference materials. Geostandards Newsletter-J. Geostandards Geoanalysis 21, 115–144.
Peccerillo, A., Donati, C., Santo, A.P., Orlando, A., Yirgu, G., Ayalew, D., 2007. Petrogenesis of silicic peralkaline rocks in the Ethiopian rift: Geochemical evidence and volcanological implications. J. Afr. Earth Sci. 48, 161–173.
Pingitore, N., Clague, J., Gorski, D., 2014. Round Top Mountain rhyolite (Texas, USA), a massive, unique Y-bearing-fluorite-hosted heavy rare earth element (HREE) deposit. J. Rare Earths 32, 90–96.
Qiu, X.F., Cai, Y.X., Jiang, T., Shan-Song, L.U., Peng, L.H., Zhao, X.M., Peng, S.G., Zhu, J., 2017. Hydrothermal alteration for the Miaoya Nb-REE deposit:constraints from C-O isotope composition of the carbonatite. Geol. Min. Resources South China 033, 275–281.
Ramsden, A.R., French, D.H., Chalmers, D.I., 1993. Volcanic-hosted rare-metals deposit at Brockman, Western Australia. Miner Deposita 28, 1–12.
Salvi, S., WilliamsJones, A.E., 1996. The role of hydrothermal processes in concentrating high-field strength elements in the Strange Lake peralkaline complex, northeastern Canada. Geochim. Cosmochim. Ac 60, 1917–1932.
Schmitt, A.K., Trumbull, R.B., Dulski, P., Emmermann, R., 2002. Zr-Nb-REE mineralization in peralkaline granites from the Amis Complex, Brandberg (Namibia): Evidence for magmatic pre-enrichment from melt inclusions. Econ. Geol. Bull. Soc. 97, 399–413.
Sheard, E.R., Williams-Jones, A.E., Heiligmann, M., Pederson, C., Trueman, D.L., 2012. Controls on the Concentration of Zirconium, Niobium, and the Rare Earth Elements in the Thor Lake Rare Metal Deposit, Northwest Territories, Canada. Econ. Geol. 107, 81–104.
Slama, J., Kosler, J., Condon, D.J., Crowley, J.L., Gerdes, A., Hanchar, J.M., Horstwood, M.S.A., Morris, G.A., Nasdala, L., Norberg, N., Schaltegger, U., Schoene, B., Tubrett, M.N., Whitehouse, M.J., 2008. Plešovice zircon — A new natural reference material for U-Pb and Hf isotopic microanalysis. Chem. Geol. 249, 1–35.
Spandler, C., Morris, C., 2016. Geology and genesis of the Toongi rare metal (Zr, Hf, Nb, Ta, Y and REE) deposit, NSW, Australia, and implications for rare metal mineralization in peralkaline igneous rocks. Contribut. Mineral. Petrol. 171, 104.
Su, J.-H., Zhao, X.-F., Li, X.-C., Hu, W., Chen, M., Xiong, Y.-L., 2019. Geological and geochemical characteristics of the Miaoya syenite-carbonatite complex, Central China: Implications for the origin of REE-Nb-enriched carbonatite. Ore. Geol. Rev. 113.
Sun, S.-S., McDonough, W.F., 1989. Chemical and isotopic systematics of oceanic basalts: implications for mantle composition and processes. Geol. Soc. London Special Publ. 42, 313–345.
Taylor, W.R., Esslemont, G., Sun, S.-S., 1995a. Geology of the volcanic-hosted Brockman rare-metals deposit, Halls Creek Mobile Zone, northwest Australia. II. Geochemistry and petrogenesis of the Brockman volcanics. Mineral. Petrol. 52, 231–255.
Taylor, W.R., Page, R.W., Esslemont, G., Rock, N.M.S., Chalmers, D.I., 1995b. Geology of the volcanic-hosted Brockman rare-metals deposit, Halls Creek Mobile Zone, northwest Australia. l. Volcanic environment, geochronology and petrography of the Brockman volcanics. Mineral. Petrol. 52, 209–230.
Thomas, R., Webster, J.D., Rhede, D., Seifert, W., Rickers, K., Förster, H.J., Heinrich, W., Davidson, P., 2006. The transition from peraluminous to peralkaline granitic melts: Evidence from melt inclusions and accessory minerals. Lithos 91, 137–149.
Trua, T., Deniel, C., Mazzuoli, R., 1999. Crustal control in the genesis of Plio-Quaternary bimodal magmatism of the Main Ethiopian Rift (MER): geochemical and isotopic (Sr, Nd, Pb) evidence. Chem. Geol. 155, 201–231.
Wang, R., Xu, Z., Santosh, M., Liang, F., Fu, X., 2017. Petrogenesis and tectonic implications of the Early Paleozoic intermediate and mafic intrusions in the South Qinling Belt, Central China: Constraints from geochemistry, zircon U-Pb geochronology and Hf isotopes. Tectonophysics 712–713, 270–288.
Wei, G.J., Liang, X.R., Li, X.H., Liu, Y., 2002. Precise measurement of Sr isotopic composition of liquid and solid base using (LP) MC-ICPMS. Geochimica 31, 295–305.
Weng, Z., Jowitt, S.M., Mudd, G.M., Haque, N., 2015. A detailed assessment of global rare earth element resources: opportunities and challenges*. Econ. Geol. 110, 1925–1952.
Wiedenbeck, M., Alle, P., Corfu, F., Griffin, W.L., Meier, M., Oberli, F., Quadt, A.V., Roddick, J.C., Spiegel, W., 1995. Three natural zircon standards for U-Th–Pb, Lu–Hf, trace element and REE analysis. Geostandards Newslett. 19, 1–23.
Williams-Jones, A.E., Migdisov, A.A., 2014. Experimental Constraints on the Transport and Deposition of Metals in Ore-Forming Hydrothermal Systems, in: Kelley, K.D., Golden, H.C. (Eds.), Building Exploration Capability for the 21st Century, 77-95.
Williams-Jones, A.E., Migdisov, A.A., Samson, I.M., 2012. Hydrothermal Mobilisation of the rare earth elements - a tale of "Ceria" and "Yttria". Elements 8, 355–360.
Xiang, Z., Yan, Q., Song, B., Wang, Z., 2016. New evidence for the ages of ultramafic to mafic dikes and alkaline volcanic complexes in the north daba mountains and its geological implication. Acta Geol. Sin. 90, 896–916.
Xiong, X., Zhao, Z., Zhu, J., Rao, B., Lai, M., 1998. Partitioning of F between aqueous fluids and albite granite melt and its petrogenetic and metallogenetic significance. Chin. J. Geochem. (English edition) 17, 303–310.
Xiong, Y., Zhong, S., Li, Z., Huang, J., Lu, X., Du, Y., Wu, E., Li, Z., Zhao, S., Zhu, Z., 2018. Geological Characteristics and prospecting potential of niobium-tantalum deposit in the Tudiling Area, Zhushan. Resourc. Environ. Eng. 32, 1–7.
Xu, C., Campbell, I.H., Allen, C.M., Chen, Y., Huang, Z., Qi, L., Zhang, G., Yan, Z., 2008. U-Pb zircon age, geochemical and isotopic characteristics of carbonatite and syenite complexes from the Shaxiongdong, China. Lithos 105, 118–128.
Xu, C., Kynicky, J., Chakhmouradian, A.R., 2010. Trace-element modeling of the magmatic evolution of rare-earth-rich carbonatite from the Miaoya deposit, Central China. Lithos 118, 145–155.
Xu, C., Kynicky, J., Chakhmouradian, A.R., Li, X., Song, W., 2015. A case example of the importance of multi-analytical approach in deciphering carbonatite petrogenesis in South Qinling orogen: Miaoya rare-metal deposit, central China. Lithos 227, 107–121.
Xu, X., Xia, L., Xia, Z., Huang, Y., 2001. Geochemical characteristics and petrogenesis of the early paleozoic alkali lamprophyre complex from Langao County. Acta Geosci. Sin. 22, 55–60.
Yang, C., Liu, C.-X., Liu, W.-L., Wan, J., Duan, X.-F., Zhang, Z., 2017. Geochemical characteristics of trachyte and Nb mineralization process in Tianbao Twonship, Zhuxi County, Southern Qinling. Acta Petrol. Et Mineral. 36, 605–618.
Ying, Y.-C., Chen, W., Simonetti, A., Jiang, S.-Y., Zhao, K.-D., 2020. Significance of hydrothermal reworking for REE mineralization associated with carbonatite: Constraints from in situ trace element and C-Sr isotope study of calcite and apatite from the Miaoya carbonatite complex (China). Geochim. Cosmochim. Ac 280, 340–359.
Ying, Y., Chen, W., Lu, J., Jiang, S.Y., Yang, Y., Ying, Y., Chen, W., Lu, J., Jiang, S.Y., Yang, Y., 2017. In situ U-Th-Pb ages of the Miaoya carbonatite complex in the South Qinling orogenic belt, central China. Lithos 290–291, 159–171.
Zhang, D., Liu, Y., Pan, J., Dai, T., Bayless, R.C., 2019a. Mineralogical and geochemical characteristics of the Miaoya REE prospect, Qinling orogenic Belt, China: Insights from Sr-Nd-C-O isotopes and LA-ICP-MS mineral chemistry. Ore. Geol. Rev. 110.
Zhang, G.W., Dong, Y.P., Lai, S.C., 2004. Mianlue tectonic zone and Mianlue suture zone on southern margin of Qinling-Dabie orogenic belt. Sci. China (Ser. D) 47, 300–316.
Zhang, G.W., Yu, Z.P., Dong, Y.P., Yao, A.P., 2000. On Precambrian framework and evolution of the Qinling belt. Acta Petrol Sin. 16, 11–21.
Zhang, G.W., Zhang, B.R., Yuan, X.C., Xiao, Q.H., 2001. Qinling Orogenic Belt and Continental Dynamics. Science Press, Beijing, pp. 1–855.
Zhang, W., Chen, W.T., Gao, J.-F., Chen, H.-K., Li, J.-H., 2019b. Two episodes of REE mineralization in the Qinling Orogenic Belt, Central China: in-situ U-Th-Pb dating of bastnäsite and monazite. Miner Deposita.
Zhu, J., Wang, L., Peng, S., Peng, L., Wu, C., Qiu, X., 2017. U-Pb zircon age, geochemical and isotopic characteristics of the Miaoya syenite and carbonatite complex, central China. Geol. J. 52.